Citation: Kahnouj, Z.J., Tangestani, M.H., Asadi, S., 2023. Insights on geochemical characteristics, microthermometry of hydrothermal fluids, and sulfur isotope systematics of the Daralu porphyry Cu deposit, SE Iran. Geologica Acta, 21.10, 1-23, I-II.
DOI: 10.1344/GeologicaActa2023.21.10

geologica acta

Insights on geochemical characteristics, microthermometry of hydrothermal fluids, and sulfur isotope systematics of the Daralu porphyry Cu deposit, SE Iran

Zahra Jalali Kahnouj **Majid H. Tangestani*** **Sina Asadi**

Department of Earth Sciences, Faculty of Sciences, Shiraz University
Adabyat Square, P.O. Box. 71454 Shiraz, Iran. Kahnouj E-mail: z.jalali@shirazu.ac.ir. Tangestani E-mail: tangstan@shirazu.ac.ir
Asadi E-mail: sinaasadi@shirazu.ac.ir

*Corresponding author

ABSTRACT

The Miocene Daralu Porphyry Copper Deposits (PCDs) is found associated with other porphyries such as Sarcheshmeh and Meiduk in the Kerman Cenozoic Magmatic Arc (KCMA), southern Iran. In this research, we provided whole-rock geochemical data, characteristics of hydrothermal fluid and sulfur isotope composition of the Daralu intrusive body, and discussed the nature, tectonic setting and fluid evolution of this deposit aiming to investigate its fertility.

The Daralu porphyry shows adakites affinity, that is, high Sr/Y and La/Yb ratios and positive Eu anomalies. The REEs patterns indicate a strong fractionation ($[La/Yb]_n$= 28.73). High La/Sm and Dy/Yb ratios suggest enrichment of amphibole and garnet as residual phases in melt source, whereas partial melting of plagioclase increases Eu and Sr in the parent magma. The presence of garnet implies a pressure equivalent to the thickness of more than 40km of crust.

To elucidate the evolutionary history of fluids and the origin of the Daralu deposit, we focused on the origin and composition of the fluid through petrography, Raman spectroscopy, and microthermometry studies of fluid inclusions. The fluid inclusions have been divided into four types: vapor (type I), aqueous-vapor (type II), CO_2-bearing (type III), and multiphase (type IV). The Raman shifts included 1284 and 1388 cm^{-1} for CO_2 and 2750–3900 cm^{-1} for H_2O. The events such as NaCl supersaturation, exhausting of CO_2-rich components, high oxygen fugacity and temperature decreasing through mineralization stages were critical in controlling the fertility of the Daralu PCD. The obtained $\delta^{34}S$ data for sulfides yielded an average of +5.5‰. Based on the observed features, it was concluded that Daralu porphyry shares formation conditions with other productive porphyries of the KCMA.

KEYWORDS | **Porphyry copper deposit. Geochemical data. Fluid inclusion. Sulfur isotopes. Daralu. Iran.**

INTRODUCTION

The Daralu Porphyry Copper Deposits (PCDs) are defined as high-tonnage, low- to medium-grade deposits (Sinclair, 2007), and they are globally the most important reserves of copper (Richards, 2015; Sillitoe, 2010). These deposits were formed by the evolution of high temperature (300–700°C) magmatic-hydrothermal fluids (Li *et al.*, 2012; Richards, 2011). The composition of hydrothermal ore-bearing fluids and their evolution are important parameters for defining the mineralization potential of an intrusive body (Li *et al.*, 2012).

It is considered that PCDs formed in arc settings related to subduction zones (Guilbert and Park, 1986; Hofmann, 1997; Wang *et al.*, 2006). Recently, it has been proposed that PCDs could be associated with continental collision margins (*e.g.* Asadi, 2018; Asadi *et al.*, 2014; Atapour and Aftabi, 2021; Haschke *et al.*, 2010; Richards, 2009; Topuz *et al.*, 2011).

A wide variety of igneous rocks have been reported responsible for PCDs formation (Singer *et al.*, 2008). An adakite-related genesis has been suggested for PCDs in post-collisional margins (*e.g.* southern Tibet: Hou *et al.*, 2015; Mao *et al.*, 2014; Yang *et al.*, 2008, and western Asia: Hezarkhani and Williams-Jones, 1998; Richards, 2015; Shafiei *et al.*, 2009). The adakitic magmas which have high potential for forming the major PCDs (Hollings *et al.*, 2005), show high ratios of La/Yb and Sr/Y, coupled with low Yb and Y, with no Eu anomalies ($Eu/Eu^{*}\geq1$). These characteristics are attributed to garnet (or amphibole) fractionation in the parental magma (Defant and Drummond, 1990; Richards *et al.*, 2012).

The Urmieh-Dokhtar Magmatic Arc (UDMA, Fig. 1A) is a well-known Cu-bearing region, where a wide range of world class porphyry copper systems have been reported and studied (*e.g.* Asadi, 2018; Atapour and Aftabi, 2021; Hassanzadeh, 1993; Hezarkhani and Williams-Jones, 1998; Khosravi *et al.*, 2019; Mohammaddoost *et al.*, 2017; Richards *et al.*, 2012; Richards, 2015; Shafiei *et al.*, 2009; Zarasvandi *et al.*, 2019). According to Zarasvandi *et al.* (2015) this is one of the best examples, in the world, of prolonged continental arcs, where the Neo-Tethys oceanic plate was subducted beneath the central Iran continental plate. There is a general consensus that, this Andean type magmatic arc (Alavi, 2004; Berberian *et al.*, 1982) was generated in response to a prolonged stage of the Neo-Tethys closure during Paleogene followed by a continental collision in Paleogene-Neogene times (Berberian *et al.*, 1982; Mohajjel *et al.*, 2003).

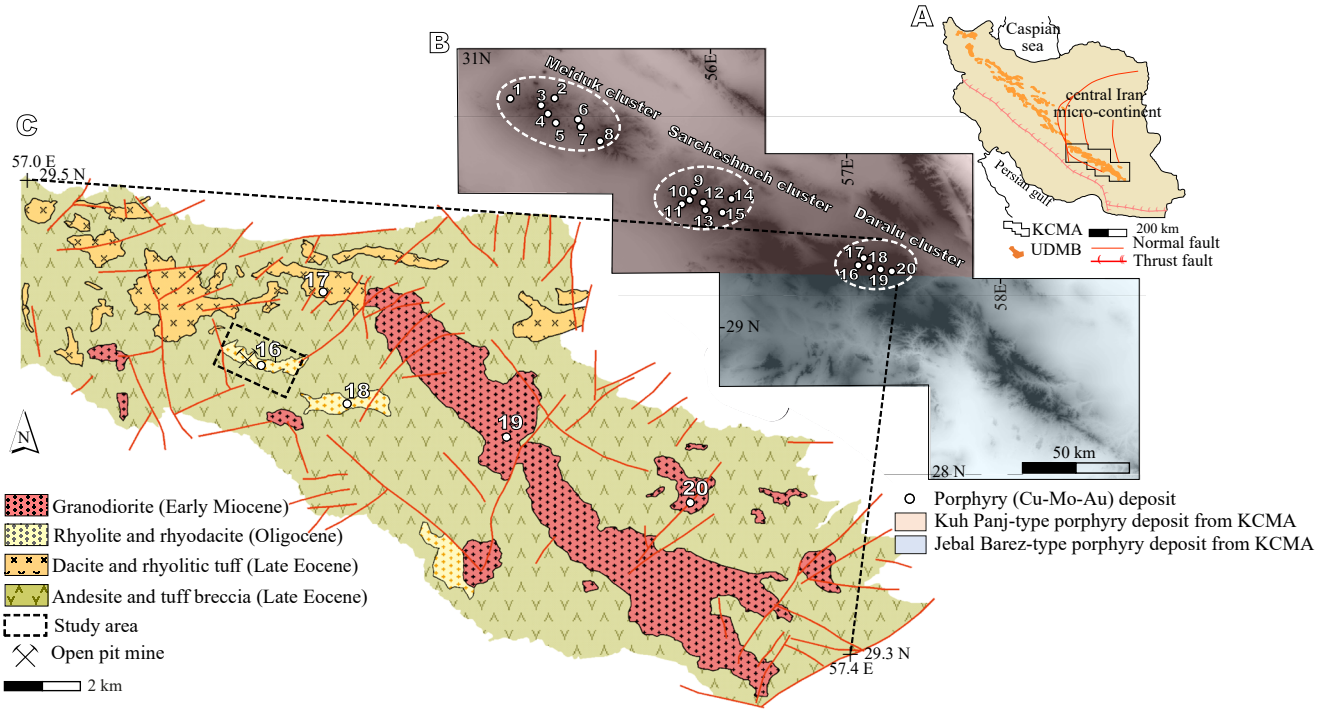

FIGURE 1. A) Geo-structural map of Iran, original from Stocklin (1968), showing location of the Kerman Cenozoic Magmatic Arc (KCMA). B) Location of the three main clusters of PCDs in the KCMA, modified after Mohammaddoost (2017), superposed on a Digital Elevation Model. C) Geological map of the Daralu area with distribution of some porphyry copper deposits or prospects which explored by NICICo, simplified from the 1:100,000 geological map of Sarduiyeh area, Iran. 1. Kader, 2. Gode-Kolvari, 3. Iju, 4. Serenu, 5. Chah-Firouzeh, 6. Parkam, 7. Meiduk, 8. Abdar, 9. Sarcheshmeh, 10. Nochoon, 11. Sarkuh, 12. Salpak, 13. Darreh Zar, 14. Kuh Panj, 15. Bagh Khoshk, 16. Daralu, 17. Babshamil, 18. Sarmeshk, 19. Bondar Hanza, 20. Gorouh.

This magmatic arc, with a length of >2000km, extends from the northwest to the southeast of Iran, as part of the western Tethyan orogenic belt (Atapour, 2017; Wang *et al.*, 2020; Zurcher *et al.*, 2019), and comprises a series of volcanic and pyroclastic Eocene rocks and Miocene–Pliocene intrusive bodies (Berberian *et al.*, 1982; Moradian, 1997).

The Cenozoic magmatic activity and the mineralization of PCDs along the UDMA are typically distributed in three main episodes: Eocene–Oligocene (Ahmadian *et al.*, 2009), middle–late Oligocene (McInnes *et al.*, 2005) and middle–late Miocene (Richards *et al.*, 2012). The major mineralization phase of porphyry systems corresponds with the southeast part of the UDMA, the Kerman Cenozoic Magmatic Arc (KCMA) of Shafiei *et al.* (2009). The copper mineralizations along the KCMA are mostly identified at late–stage Miocene granodiorite that has adakitic affinity, compared to that of Eocene–Oligocene intrusions (Afshooni *et al.*, 2013; Asadi *et al.*, 2014). The three main PCDs of Miocene granodiorite in the KCMA are Sarcheshmeh, Meiduk and Daralu (Mohammaddoost *et al.*, 2017; Fig. 1B).

The Daralu PCD with 186Mt of ore at 0.36% Cu (Mineral Resources Data System of United States Geological Survey, 2015), occurs in the central part of the KCMA, 150km southeast of the Sarcheshmeh supergiant deposit (Fig. 1B). The first exploratory study in the Daralu area was carried out by Charter (1971), which was recently followed by the Company of National Iranian Copper Industries (NICICo).

The tectonics, magmatism, petrology and geochemistry of KCMA have been studied by several authors (Asadi *et al.*, 2014; Atapour and Aftabi, 2021; Bomeri *et al.*, 2010; Dimitrijevic, 1973; Mohammaddoost *et al.*, 2017; Richards *et al.*, 2012; Shahabpour, 2005; Shafiei *et al.*, 2008, 2009, 2010; Zarasvandi *et al.*, 2015). Most of these studies were focused on its northwestern area, where two important PCDs, Sarcheshmeh with 1200Mt of sulphide ore at an average grade of 1.2% Cu (Ellis, 1991) and Meiduk with 500Mt of ore, at 0.86 wt.% Cu (Aghazadeh *et al.*, 2015) are located. The size, abundance, and tonnage of PCDs broadly increase from southeastern to northwestern the KCMA, and the majority of economic PCDs are situated in the northwestern sector (McInnes *et al.*, 2005; Shafiei *et al.*, 2009). Asadi (2018) reported the geochemical characteristics of granitoids in the northern part of KCMA, which were: high SiO_2 (>69.5%), K_2O (>2.8%), low MgO (<1.4%), high Sr/Y (>60.9%) and La/Yb (>20%) ratios, relatively low Mg# (<42.6%) and compatible elements (*e.g.* Cr≤ 21.6ppm). However, scarce information has been reported on the geological features and copper deposits of central and southern parts of KCMA (Hezarkhani, 2006; Hosseini *et al.*, 2017).

Recently, NICICo (2021), based on new drilling cores, has reported 194Mt of ore at 0.38% Cu for the Daralu deposit in the central part of KCMA. The major objective of the present work was to investigate the geochemistry and characteristics of the magmatic hydrothermal fluid that led to the fertility of this deposit.

GEOLOGY

Shahabpour (2005) suggested that the subduction of the Neo-Tethys oceanic slab under the Central Iran microcontinent during the Eocene (before the collision) originated a magmatic arc of calc-alkaline to tholeiitic nature. Ghasemi and Talbot (2006) stated that the increase of convergence rate of Eurasian and Arabian plates as a result of the opening of the Red Sea from the Middle Oligocene affected the convergence and final collision of the Arabian plate with the Central Iran microcontinent. The termination of the continental collision during the Paleogene was followed by the tension, magmatic activity and over thrusting of the KCMA (McClay *et al.*, 2004). Rb-Sr dating in combination with the geochemical data of the KCMA granitoids indicate an age of 33Ma (Dargahi *et al.*, 2010), which matches the beginning of the collision between the Arabian plate and the Central Iran microcontinent.

The KCMA consists of several magmatic complexes of different nature such as the Bahr-e-Asman complex (77.51±0.81Ma; ~7km in thickness) composed of basaltic andesite and andesitic lava flows and intermediate-felsic plutons (Hosseini *et al.*, 2017); the Razak complex (37.5±1.4Ma; ~7.5km in thickness) composed mainly of basaltic-rhyolitic volcanoclastics displaying calc-alkaline/tholeiitic signatures (Ahmad and Posht Kuhi, 1993; Hassanzadeh, 1993); and the Hezar complex (32.7±6.3Ma; ~1.4km in thickness) made up of trachyandesite and trachybasalt with calc-alkaline intrusions (Hassanzadeh, 1993; Shafiei *et al.*, 2009). These complexes were formed during the 60-million-year history of the arc during the Cenozoic (Shafiei *et al.*, 2009). The intensity and spread of mineralization in the KCMA correspond to the incidence rate and distribution intensity of intrusive bodies. The central and northwestern segments of the arc contain Miocene adakitic-oriented granitoids associated with economic porphyries regionally recognized as Kuh Panj-type (KP) (Shafiei *et al.*, 2009). In contrast, the southeastern segment of this arc contains calk alkaline granitoids associated with barren or subeconomic porphyry copper mineralization regionally recognized as Jebal Barez-type (JB) (Shafiei *et al.*, 2009). Asadi *et al.* (2014) and Shafiei *et al.* (2009) estimated that the thickness of the crust is >40 to 50km in the KP and 30 to 40km in the JB, suggesting that the adakitic features have a connection with the thickened lower crust.

There are three main clusters of porphyry copper systems in the KCMA, from northwest to the southeast: Meiduk (*e.g.* Meiduk, Kader, Iju, Chah-Firouzeh, Serenu, Parkam), Sarcheshmeh (*e.g.* Sarcheshmeh, Nochoon, Darreh Zar) and Daralu (*e.g.* Daralu, Babshamil, Sarmeshk, Bondar Hanza, Gorouh) (Mohammaddoost *et al.*, 2017; Fig. 1B). The major PCDs are Sarcheshmeh (13.20Ma), Meiduk (11.58Ma) and Daralu (12.96Ma) (Aghazadeh *et al.*, 2015).

The Daralu area is outlined in the 1:100,000 geological map of the Sarduiyeh area (Hosseinjani Zadeh and Tangestani, 2011). The dominant lithological units in the Daralu area are the Eocene andesites and tuffs of the Razak Formation (Atapour, 2007), typically intruded by Miocene granodiorites (Mohammaddoost *et al.*, 2017; Fig. 2A). Another common geological feature of the study area is the occurrence of fracturing systems intruded by late barren diabasic and andesitic dykes, already reported around other mineralized stocks of the KCMA (Hassanzadeh, 1993; Shahabpour, 1992; Taghipour *et al.*, 2008).

The mineralized and altered stock at Daralu is visible on a surface of approximately 0.7km^2, which is elongated within 1.2km long NW–SE trending corridor. Several types of hydrothermal alterations based on drillhole logs, outcrop observations, and thin sections and polished samples have been observed (Fig. 2B). They are grouped into three distinct types of mineralization, including hypogene, supergene and leached (Habibi and Hezarkhani, 2012): i) hypogene zone: the highest Cu values occur at depths of 120m to at least 240m below the present erosional surface, that is the boundary between the potassic and phyllic alterations with weak mineralization in the propylitic alteration; ii) supergene zone: this zone is not well-distributed in the area and its thickness is variable; iii) leached zone: the thickness of the oxidized-leached zone is 2–25m with about 0.2% Cu on average (Habibi and Hezarkhani, 2012). The hydrothermal alterations in the area are: i) potassic, with potassium feldspar and biotite as predominant minerals; ii) phyllic, characterized by pyrite veins and alteration of biotite and feldspar into sericite (Fig. 3A); iii) argillic, characterized by alteration of feldspar into kaolinite or smectite; and iv) propylitic, with dominant epidote, chlorite and calcite.

The hypogene zone is comprised of pyrite, chalcopyrite, magnetite, bornite and tetrahedrite, mostly in the stockwork and replacement forms (Fig. 3G). The undeveloped supergene zone consists of covellite, chalcocite, hematite, goethite, malachite, azurite, chalcanthite and pyromorphite. The mineral assemblage of leached zone mainly consists of Fe–oxides and hydroxides (goethite, hematite and limonite). The copper mineralization occurs mainly at the boundary of potassic and phyllic alterations (Habibi and Hezarkhani, 2012).

ANALYTICAL METHODS

Forty samples from outcrops and bore holes from the Daralu deposit were collected for microthermometry, isotopic, and major and trace elements analyses.

Polished thin sections of altered and fresh samples were prepared for microscope studies. Fresh samples were also selected for whole-rock geochemical analysis.

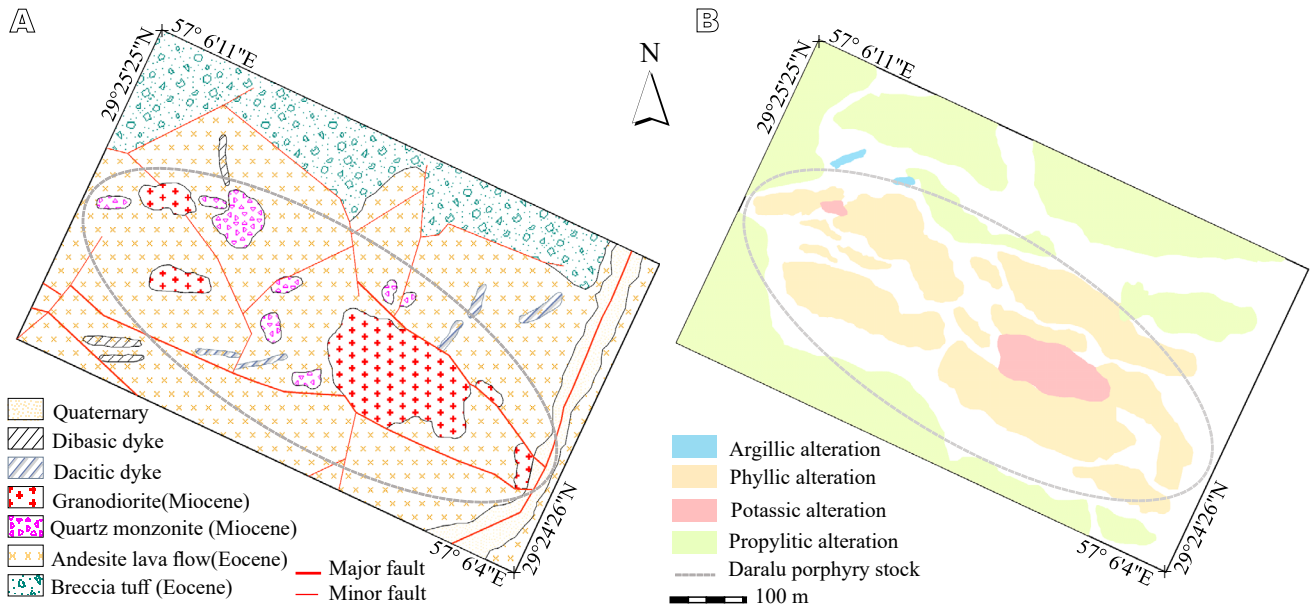

FIGURE 2. A) 1:1,000 Geological map and B) alteration map of the Daralu PCD, modified after NICICo (2010).

For geochemical analysis, samples of large particle size were jaw crushed to a nominal 6mm size before being puerized in a ring-and-punch mill to a nominal minus 75μm grind-size.

Alkaline fusion and Inductively Coupled Plasma Mass Spectrometry (ICP-MS), advanced functional materials (AFMS) package were used to analyze major and trace elements, and Rare Earth Elements (REEs) at the Zarazma Mineral Studies Company, Iran.

Nine pyrite and chalcopyrite samples, separated manually from crushed samples using a binocular microscope, were analyzed in the Stable Isotopes Research Laboratory, Arak University, Iran, to measure the sulfur isotopes. After combustion of a sulfide sample in an elemental analyzer at 1150ºC, the generated SO_2 gas was passed through the system which was stripped of water and SO_2. The adsorption column was then heated to 220ºC to release any accumulated SO_2. This gas was ultimately exerted into the Isotope-Ratio Mass Spectrometer (IRMS). During the spectrometry, mass ratio of 66/64 was determined to evaluate the ratio of $^{34}S/^{32}S$

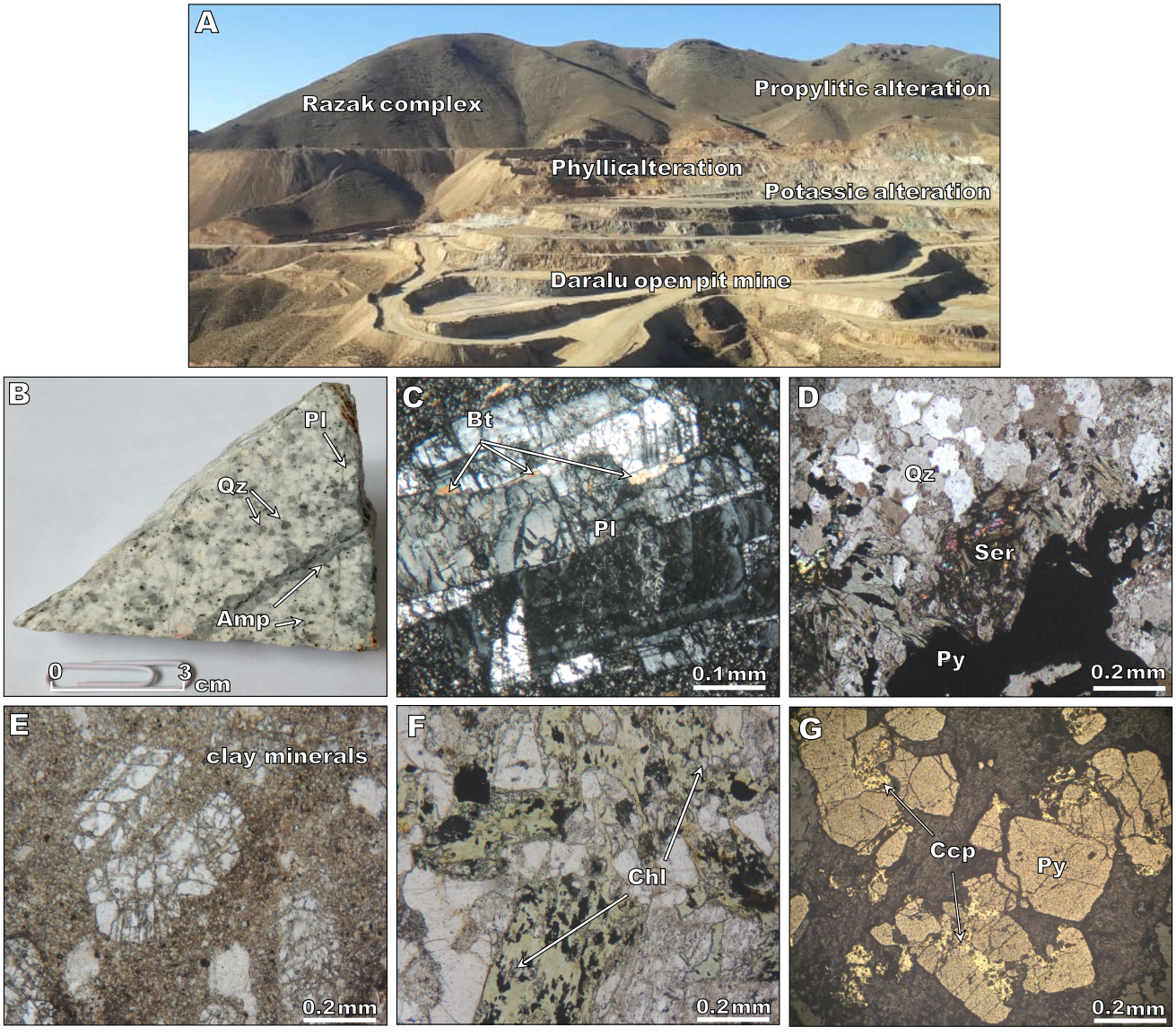

FIGURE 3. A) Field photograph of Daralu alteration zones in the volcanic rocks of the Razak Complex (view to north). B) Hand specimen of granodiorite from the Daralu intrusive body. Photomicrographs of C) potassic alteration with replacement of plagioclase by hydrothermal biotite Crossed Polarized Light (XPL), D) phyllic alteration consisting of quartz, sericite and pyrite (XPL), E) argillic alteration which show plagioclase replaced by clay minerals Plain Polarized Light (PPL), F) chloritization in the propylitic alteration (PPL) and G) replacement of pyrite by chalcopyrite in reflected light. Mineral abbreviations (Whitney and Evans, 2010): Amp= amphibole, Anh= anhydrite, Bt= biotite, Cal= calcite, Ccp= chalcopyrite, Chl= chlorite, Mag= magnetite, Pl= plagioclase, Py= pyrite, Qz= quartz, Ser= sericite.

of the sample. To verify the whole procedure and to calibrate the reference gas, repetitive measurements were performed on the basis of reference material of International Atomic Energy Agency (IAEA-S-4) and a secondary standard. The certified $\delta^{34}S$ (‰) value for IAEA-S-4 standard is +16.9±0.2 vs Vienna-Canyon Diablo Troilite (VCDT) and the accepted $\delta^{34}S$ (‰) value for the secondary standard is -6.3±0.16 vs VCDT. The accepted instrumental value for $\delta^{34}S$ standard deviation (1σ) is 0.20‰.

The Daralu PCD hydrothermal veins were considered suitable for the study of Fluid Inclusions (FIs). Thirteen quartz samples showing early, main and late stages of mineralization were collected for petrography, Raman spectroscopy and microthermometry.

Microthermometric analyses were conducted on THMSG600 model of Linkam stage attached to a Leica petrographical microscope at -190 freezing temperature to 600ºC heating temperature in the Iran Mineral Processing Research Center (IMPRC). The heating rates were 1ºC/min for measurements of homogenization temperatures (T_h total). The accuracy of temperature measurements was ±2ºC during heating and ±0.2ºC during freezing. Vapor volumetric percent within FIs was estimated at ~25ºC (room temperature) using standard graphical charts (Shepherd *et al.*, 1985). The last melting temperature of ice (T_m (Ice)) was used to calculate the salinities as wt.% NaCl equivalent (eqv.) for the two-phase aqueous inclusions (Bodnar, 1993), dissolution temperatures of daughter minerals (T_h (Halite)) for the multiphase-bearing inclusions (Hall *et al.*, 1988) and final melting temperatures of CO_2-rich phases (T_m (Clath)) for the clathrate-bearing inclusions (Collins, 1979). The pressure and bulk fluids (ρb) were computed in the FLUIDS program (Bakker, 2003). Calculations of pressure range, homogenization conditions and density of mixed aqueous-carbonic phase were made using published Equations Of State (EOS): Bowers and Helgeson (1983) for H_2O-CO_2-NaCl FIs, and Zhang and Frantz (1987) for H_2O-NaCl FIs in the FLUIDS based on Fls volumetric data (P-V-T-X). The representative fluid inclusions were examined to confirm the vapor and liquid compositions of single inclusions using a LabRAM HR Evolution laser Raman spectroscopy system with a laser source of 532.2nm at Shiraz University, Central Laboratory. The spectral region starts from 50cm^{-1}, with a spatial resolution of ±2μm, applying the method of Burke (2001).

RESULTS

Petrography

The composition of the Daralu granodiorite was determined based on the study of polished thin sections prepared from logs of 152 drill holes. Results showed a porphyritic rock with anhedral quartz, euhedral plagioclase and subhedral K-feldspar as dominant felsic minerals and biotite and amphibole as mafic constituents (Fig. 3B). The plagioclase clearly shows normal zoning and polysynthetic twinning, while the K-feldspar reveals carlsbad twinning. Magnetite, apatite, zircon and titanite are present as accessory minerals.

Potassic alteration, the early hydrothermal alteration, is associated with mineralization, and is observed in small patches in the center of the deposit and in deep drill cores. This alteration consists of secondary biotite, orthoclase, magnetite, anhydrite and quartz as major phases, and tremolite-actinolite and opaque minerals as minor minerals (Fig. 3C). The phyllic alteration is widespread in the Daralu district, specified by the presence of sericite, quartz, pyrite and disseminated chalcopyrite in deep regions. Sericite replaces plagioclase and amphibole (Fig. 3D). The argillic alteration, clay minerals that replace K-feldspar and plagioclase (Fig. 3E), occurs as small patches at the northwestern part of the district. X-Ray Diffraction (XRD) analysis indicates that the argillic alteration minerals are, in an order of frequency, kaolinite, illite, muscovite, albite, montmorillonite and jarosite. The propylitic alteration is the more extensive alteration and is present in deep regions of the northern drill cores. Propylitic assemblage includes epidote, chlorite, albite and calcite (calcite and chlorite have replaced the biotite) (Fig. 3F).

Post-mineralization dykes of predominant dacite composition, cut intrusive phases in the northwest of the area. These rocks display sub-aphanitic texture and are mainly composed of fine crystals and a few phenocrysts and are altered with variable intensity. A few occurrences of Fe hydroxides are observed in the fractured rocks. Plagioclase and clinopyroxene are the major phenocrysts in the dyke rocks. The clinopyroxene crystals are generally euhedral and sometimes altered to epidote, chlorite and quartz and rarely to tremolite–actinolite. Recrystallization is dominant in mafic minerals, while argillic and silicic alterations are no significant.

Examination of samples from 152 drilling cores by the NICICo shows that the highest hypogene mineralization (chalcopyrite, pyrite and bornite) occurs at depths of 110m to <230m at the potassic alteration zone (about 0.15wt.% Cu) and at the boundary of potassic and phyllic alterations (about 1.8wt.% Cu). Mineralization has occurred in stockwork and dissemination forms.

According to Sillitoe (2010) and crosscutting relationships between early, main and late mineral phases, four major types of veins are distinguished in the Daralu deposit. i) M-type veins: they formed during

the pre-ore (early) stage, occur in the deep regions of the potassic alteration zone, and consist of quartz, magnetite, anhydrite and sporadic chalcopyrite (Fig. 4A). ii) A-type veins: as the main ore-stage indicators, they are found in the potassic-phyllic alteration zone and in the interior of the propylitic alteration zone, and consist of quartz, chalcopyrite, K-feldspar, pyrite and traces of molybdenite (Fig. 4B). iii) D-type veins: they are thick and the most abundant veins observed in the phyllic alteration zone, characterized by quartz and pyrite with minor sericite and chalcopyrite (Fig. 4C), early and main quartz veins/veinlets being intruded by D-type late veins/veinlets (Fig. 4E); iv) L-type veins: they consist of quartz and calcite free of mineralization and evidence the ultimate hydrothermal activity. They are generally observed in the near-surface areas of the propylitic and phyllic alteration zones where they crossed older veins (Fig. 4D). Table 1 displays the characteristics of vein types in the Daralu deposit.

Geochemical composition

To determine the petrogenesis and geochemical affinity of the Daralu porphyry, the whole- rock compositions of 13 samples collected from the intrusive body were analyzed. The abundances of major oxides and trace elements along with the significant ratios and indexes are listed in Table I, Appendix.

The scheme of major element oxides on the Alkali vs. SiO_2 diagram (Middlemost, 1994) shows that they could be categorized in granodiorite and quartz monzonite rock types (Fig. 5A).

The Daralu porphyry stock samples are located in the calc-alkaline field of the AFM diagram of Irvine and Baragar (1971) (Fig. 5B). On the K_2O vs. SiO_2 diagram of Peccerillo and Taylor (1976), the Daralu rocks are within the high-K calc-alkaline series field (Fig. 6A). Moreover, all samples show high Alumina Saturation Indices (ASI) with average of 1.01 which corresponds to the field of peraluminous and I-type in the diagram of SiO_2 vs. ASI (Maniar and Piccoli, 1989; Fig. 6B).

Sulfur isotopes

The $\delta^{34}S$ values measured for pyrite (n= 7) of D-type veins show a range of 4.7 to 6.8‰, and for chalcopyrite (n= 2) of A-type veins a narrow range from 5.7 to 6.0‰. Results revealed that the $\delta^{34}S$ average is 5.5‰ (Table 2). There is not significant difference between sulfur isotopic compositions of sulfides in samples of A- and D- type veins (Table 2).

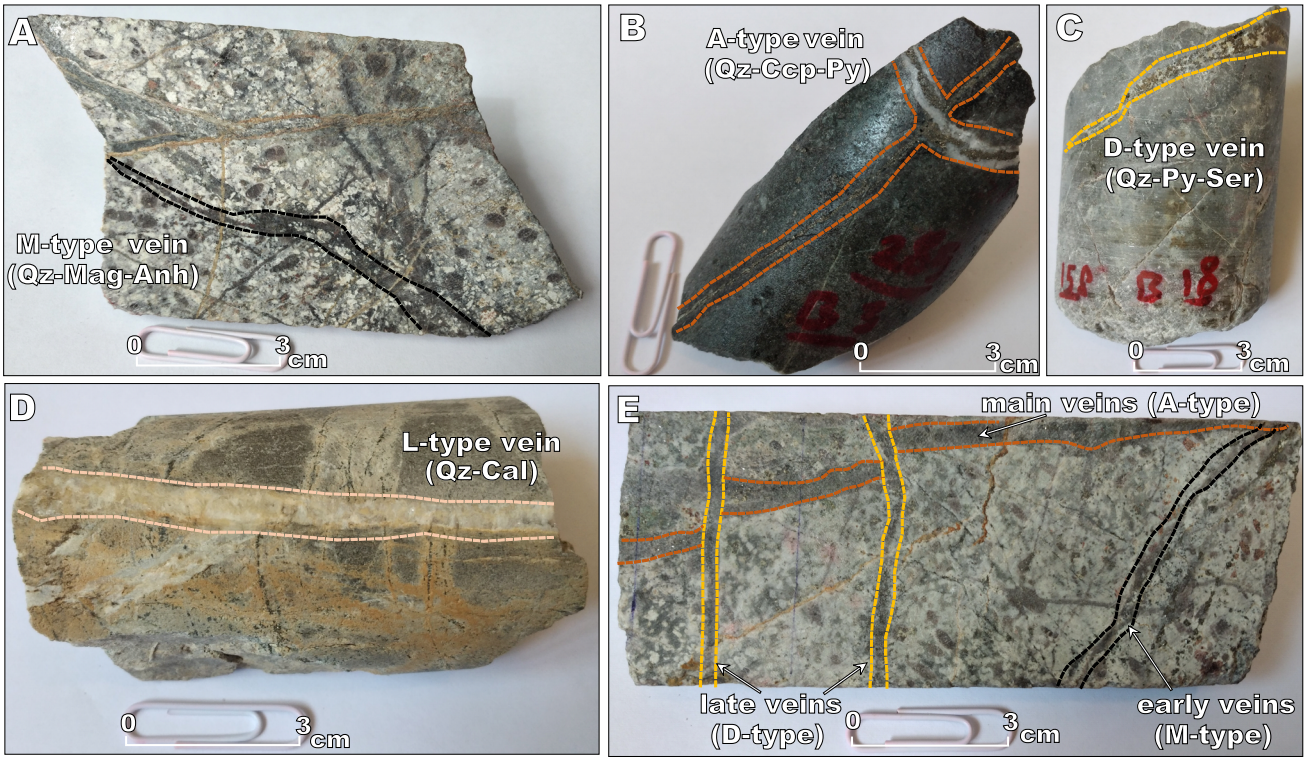

FIGURE 4. Vein types in the photographs of core crosscutting. A) M-type vein as the early vein in the potassic alteration. B) A-type vein as the main sulfide mineralization vein in inner propylitic alteration. C) D-type vein as the thick late vein in the phyllic alteration. D) L-type carbonate vein. E) relationships of the various veins crosscutting. The A-type vein cut by the D-type but crosscut the M-type vein. Abbreviations as in Figure 3.

TABLE 1. The major oxides and trace elements data as well as important ratios of trace elements of Daralu porphyry intrusive body

Vein type	Alteration	Depth (m)	Vein's width (mm)	Mineral assemblage
M type	depth potassic	>220	<1–5	Qz + Anh + Mag ± Mol ± Ccp ± Bn ± Py
A type	potassic imprinted by phyllic and interior propylitic	~100–210	1–15	Qz + Ccp + Kfs + Py
D type	phyllic	~40–90	2–35	Qz + Py ± Ser ± Ccp
L type	phyllic and propylitic	close to the surface	<1–25	Qz + Cal ± Gyp

Anh= Anhydrite, Bn= Bornite, Cal= Calcite, Ccp= Chalcopyrite, Gyp= Gypsum, Kfs= K–feldspar, Mag= Magnetite, Mol= Molybdenite, Py= Pyrite, Qz= Quartz, Ser= Sericite

Fluid inclusions

Petrography and classification

The FIs petrography was examined for 13 double polishing sections of quartz vein types M, A and D, and the FIs were classified based on the phase's frequency at ~25ºC using Van den Kerkhof and Hein (2001) method. FIs are divided into vapor (type I), aqueous-vapor (type II), aqueous-carbonic (CO_2-bearing, type III) and multiphase (type IV) types (Fig. 7), according to petrographic and microthermometric studies.

Type I FIs are mono phase gaseous inclusions with a mono phase of vapor (V); these are relatively common in vein type A and are mostly observed in spherical and irregular shapes from 2 to 15 microns in dark color (Fig. 7A).

Type II FIs are two phases, liquid rich (LV, Fig 7B) and vapor rich (VL) inclusions among which, the LV type is dominant in all the vein types occurring as primary individual and cumulative inclusions. The vapor phase occupies about 10 to 30% of the inclusions and predominantly homogenizes to the liquid phase. These inclusions have elliptical and irregular shapes with a size of 5 to 30 microns. The coexistence of the LV and V inclusion types indicates the boiling process (Simmons *et al.*, 2000) (Fig. 7A). The VL type inclusions, with a frequency less than liquid-rich inclusions, were observed in vein types A and D, as well. Moreover, the water vapor phase involves about 70% to 95% of the volume of inclusion. These inclusions show similar shape and size to the LV type.

Type III FIs consist of immiscible H_2O and CO_2 phases along with vapor (L_1L_2V), rarely occurring (Fig. 7C, D). Type IV are multi-phase liquid-vapor-

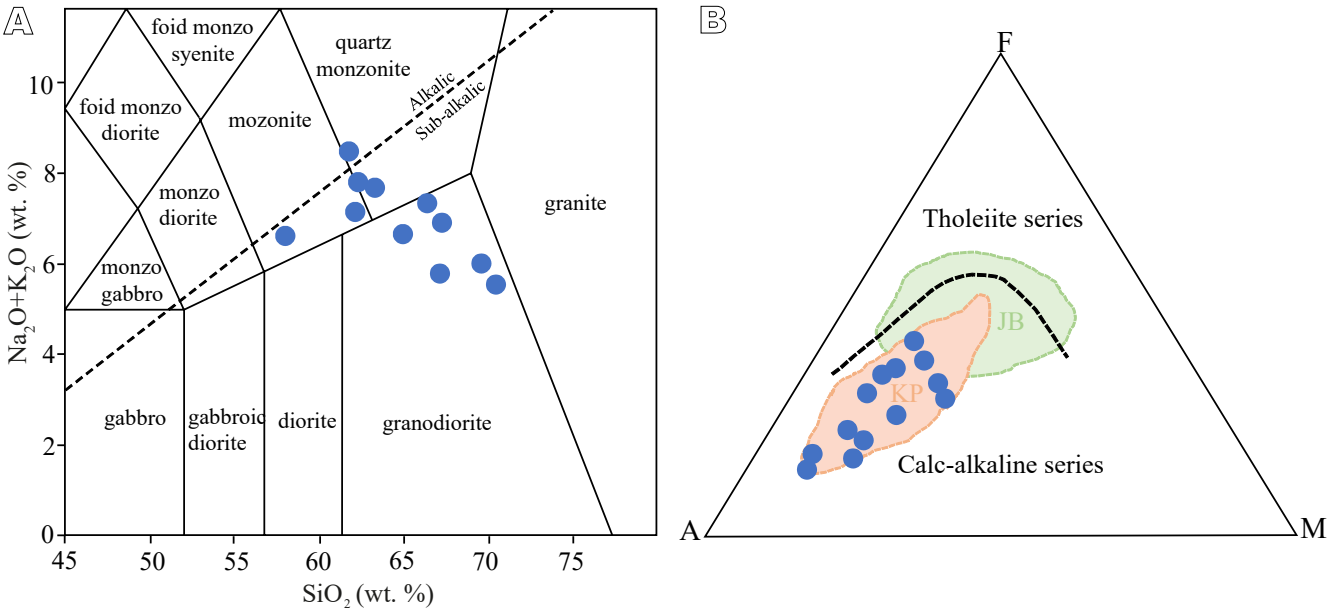

FIGURE 5. Plots of Daralu samples. A) Total Alkali vs. Silica (TAS) classification diagram (Middlemost, 1994). B) Alkali-FeOt-MgO (AFM) diagram (after Irvine and Baragar, 1971). The Kuh Panj (KP) and Jebal Barez (JB) fields are from Shafiei *et al.* (2009).

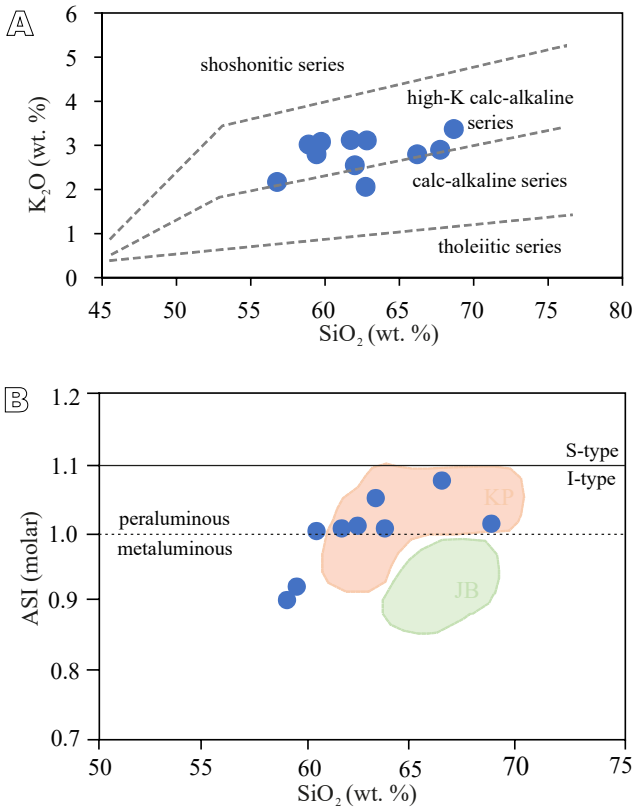

FIGURE 6. Plots of Daralu samples. A) K_2O vs. SiO_2 diagram (Peccerillo and Taylor, 1976). B) ASI (Al_2O_3 /CaO + K_2O + Na_2O) vs. SiO_2 (after Maniar and Piccoli, 1989). The Kuh Panj (KP) and Jebal Barez (JB) fields are from Asadi *et al.* (2014).

halite-solid (LVHS) FIs consisting of liquid, vapor and variable proportions of daughter-solid phases. Halite and sylvite are predominant, and occasionally accompanied with daughter phase; therefore, halite-rich FIs are almost all FIs measured. The solid phases (*e.g.* hematite and chalcopyrite) and some unidentified opaque phases rarely constitute >1% volume of an inclusion and therefore, do not affect T_h. These inclusions are observed individually in all veins with sizes of about 10 to 15 microns. The association of LVHS and VL inclusions (Fig. 7E, F) offers two immiscible fluids with one primary origin.

Microthermometric and laser Raman results

Microthermometric analyses were performed on 70 primary and pseudosecondary FIs approximately >7 microns in size. Microthermometric characteristics of type II, type III and type IV inclusions from early, main and late ore stages are listed in Table 3.

The type IIA inclusions yield first ice-melting temperatures (T_e (Ice)) varied from -30 to -21ºC. The range of homogenization temperatures (T_h) of type II (LV) FIs varied from 451ºC to 580ºC in the early stage, and from 210ºC to 310ºC in the late stage, whereas T_h values of type III (L_1L_2V) varied from 370ºC to 529ºC and 246ºC to 302ºC in the early and main stages respectively, and from 217ºC to 395ºC in type IV (LVH±S) in the main stage. The type II FIs yield last ice melting temperatures (T_m (Ice)) from -19ºC to -5ºC and from -16ºC to -4ºC in early and late stages of mineralization, respectively. The type IV yields final halite dissolution temperatures (T_m (Halite)) from 180ºC to 340ºC in the main stage. These temperature values indicate salinity range of 7.9 to 21.7, 35.9 to 55.9 and 5.7 to 18.9wt.% NaCl eqv. for FIs in early, main and late ore stages, respectively.

Bulk densities of FIs are calculated for the mentioned stages ranging from 0.97 and 1.07, from 1.04 and 1.36, and finally from 0.95 and 1.03g/cm^3. The range of CO_2 melting temperatures (T_m (CO_2)) in the type III inclusions (L_1L_2V) varied from -61ºC to -59ºC and -58ºC to -50ºC in early and main stages, respectively. The clathrate melting (T_m (Cla)) range is from 3ºC to 8ºC, and corresponding salinities are 2.9 to 11wt.% NaCl eqv. in the early type III of FIs. Moreover, the T_m (Cla) range is from 2ºC to 10ºC, and corresponding salinities are 3 to 12.2 wt.% NaCl eqv. in the main type III of FIs. The

TABLE 2. Sulfur isotope data for pyrite (Py) and chalcopyrite (Ccp) samples collected from Daralu deposit

Sample no (Sample Analyzed Name)	Mineralogy	$\delta^{34}S$ (‰) V−CDT (‰) ±1σ
1 (Dau187−116)	Py	+4.79 ± 0.12
2 (B 16−120)	Py	+4.76 ± 0.11
3 (B2−170)	Py	+6.06 ± 0.08
4 (Ash−30)	Py	+5.11 ± 0.15
5 (B18−105)	Py	+6.00 ± 0.19
6 (B3−280)	Py	+6.75 ± 0.14
7 (Dau (p) −286)	Ccp	+5.71 ± 0.20
8 (Dau 172−114)	Py	+4.69 ± 0.06
9 (Dau (p)−45)	Ccp	+6.02 ± 0.11
average		+5.54

Isotopic data of sulphides (or sulfides). See Table 1 for abbreviations

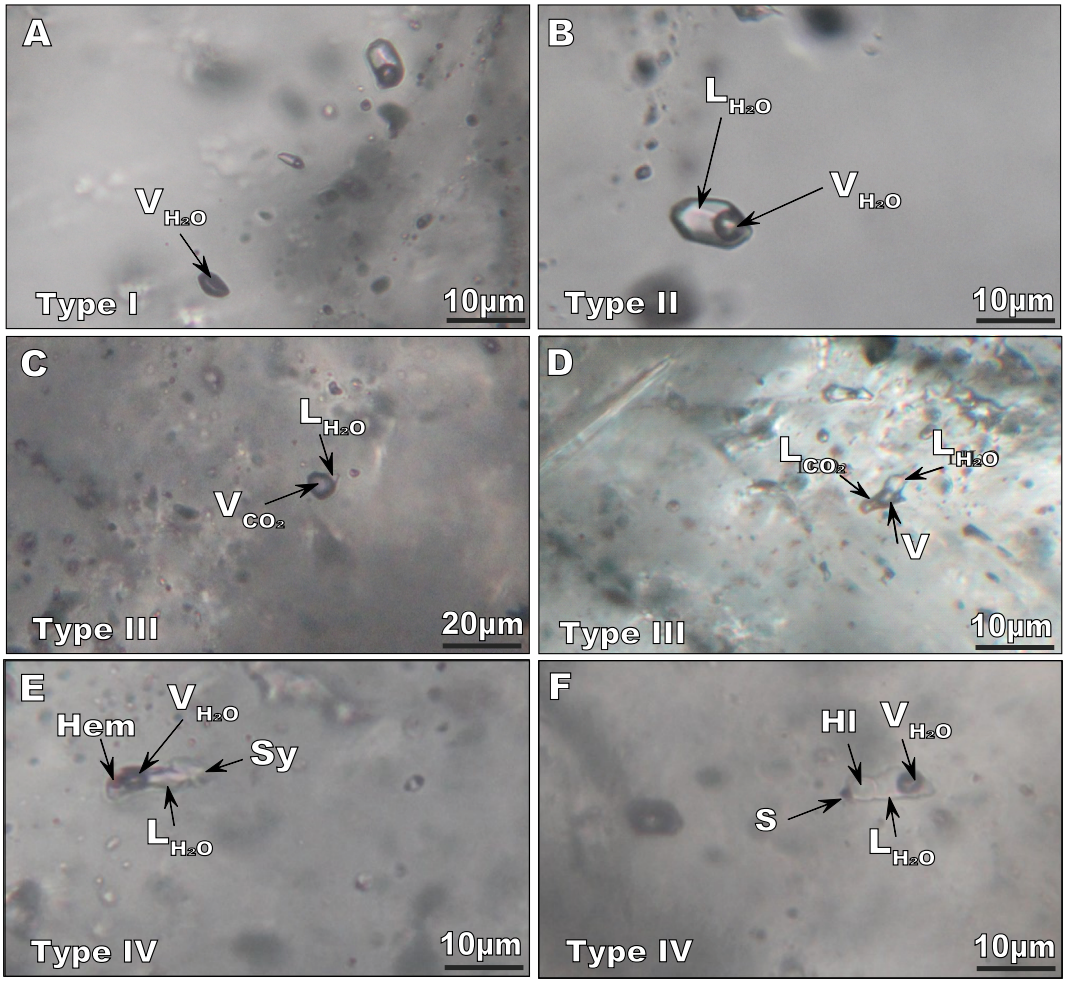

FIGURE 7. Photomicrographs of inclusion in quartz veins of the Daralu deposit. A) Type-I, mono-phase Vapor (V). B) Type-II, two-phase aqueous Liquid-Vapor (LV). C) and D) Type–III, CO2– bearing inclusion (L1L2V). E) and F) Type-IV, multi-phase halite-baring (LVH±S). Abbreviations: L= liquid, V= vapor, Hl= halite, Hem= hematite, Sy= sylvite, S= solid.

homogenization temperatures of CO_2 (T_h (CO_2)) in the type III FIs of early stage are between 21ºC and 30ºC. The bulk densities of aqueous-carbonic FIs range from 0.82–0.88 and 0.89–0.93g/cm^3 in early and main stages, respectively.

According to the microthermometric data in quartz veins, three groups of FIs were defined: group 1, with high homogenization temperature (T_h) (451ºC–580ºC) and low to moderate salinity (7.9–21.7wt.% NaCl equivalent); group 2, with moderate to high T_h (217ºC–395ºC) and high salinity (35.9–55.9wt.% NaCl equivalent), and group 3, with low T_h (210ºC–310ºC) and low salinity (5.7–18.9wt.% NaCl equivalent). Therefore, the main stage of copper mineralization is related to the group 2.

Laser Raman Spectroscopy (LRS) was used as a non-destructive method for qualitative detection of gaseous phases in type III FIs of veins type A that were likely to contain CO_2 according to petrographic studies. The main recorded Raman shifts (Frezzotti *et al.*, 2012) included 1284 and 1388cm^{-1} for CO_2, 2750–3900cm^{-1} for H_2O liquid and 3657–3756 cm^{-1} for H_2O vapor (Fig. 8). This feature is according to the T_m (CO_2) results (-61 to -59 and -58 to -50ºC, Table 3).

According to microthermometric studies and Raman spectroscopy analyses, in the late-stage H_2O is the major phase of type II FIs, indicating that an aqueous solution was responsible for the waning stage of Daralu PCD.

Laser Raman spectroscopy indicates (Fig. 8) overlapping bands in the 2750 to 3900cm^{-1} of OH stretching region. As depicted by Sun (2009), this feature shows interplay of water molecules with the neighbor molecules. According to Frezzotti (2012), chlorine ions break hydrogen bonds in aqueous phases, which effects the variation of OH stretching bands.

TABLE 3. Measurement microthermometric parameters of 70 fluid inclusions

Stage (Inclusion types)	Phases	T_e (Ice) (°C)	T_m (Ice) (°C)	T_m (Cla) (°C)	T_m (CO_2) (°C)	T_h (CO_2) (°C)	T_m (Halite) (°C)	wt. % NaCl eqv.	T_h (°C)	(ρbulk) (g/cm^3)	Pressure (bars)
Early (type−II)	LV	−30 to −21	−19 to −5	---	---	---	---	7.9–21.7	451–580	0.97–1.07	---
Early (type−III)	L_1L_2V	---	---	3 to 8	−61 to −59	21–30	---	2.9 to 11	370 to 529	0.82– 0.88	1053–1450
Main (type−III)	L_1L_2V	---	---	2–10	−58 to −50	---	---	3–12.2	246–302	0.89– 0.93	980–1235
Main (type−IV)	LVH±S	---	----	---	---	---	180–340	35.9–55.9	217–395	1.04–1.36	---
Late (type−II)	LV	−30 to −21	−16 to −4	---	---	---	---	5.7–18.9	210–310	0.95–1.03	---

Notes: T_e(Ice): eutectic temperature; T_m(Ice): final ice melting temperature; T_m(Cla): dissolution temperature of CO_2 clathrate; T_m(CO_2): melting temperature of CO_2 phase; T_h(CO_2): homogenization temperature of CO_2 phase into the carbonic vapour phases; T_h: homogenization temperature; L_1: H_2O−liquid; L_2: CO_2−liquid; V: vapour; S: solid phases and H: halite. Fluid inclusion terminology and symbols according to Diamond (2003).

DISCUSSION

Geochemical affinity

In terms of geochemical characteristics, the Daralu samples show adakitic-like compositional features (Richards and Kerrich, 2007) with high concentrations of Sr (>400ppm), Na_2O (>3.5wt.%), Al_2O_3 (>15wt.%), Sr/Y ratio >20, La/Yb ratio >20, and low concentration of Y (<18ppm, Table 4). All samples are located in the adakitic range in Sr/Y vs. Y diagram (Defant and Drummond, 1990; Fig. 9C) showing the partial melting trend of a source containing garnet. Moreover, according to the Y vs. SiO_2 and La/Yb vs. SiO_2 diagrams (Richards and Kerrich, 2007; Richards *et al*., 2012; Fig. 9A, B), most studied samples are plotted in the adakite field.

High La/Yb (>37) and Sr/Y (>78) ratios of the Daralu PCD indicate Light Rare Earth Elements (LREEs) enrichment comparative to Middle and Heavy Rare Earth Elements (MREEs and HREEs, respectively) (Table I, Appendix; 5) due to the garnet, clinopyroxene and hornblende occurrences in the melt source (Castillo, 2012; Martin *et al.*, 2005; Peacock *et al.*, 1994). Apparently, the Daralu granitoid is the product of partial melting of mafic rocks with garnet presence (low HREEs+Y) and the plagioclase absence (high Sr) which commonly intrudes in a post-collisional setting (Richards *et al.*, 2012). Depending on the geodynamic context, these conditions usually prevail at depths of more than 30km (Castillo, 2012).

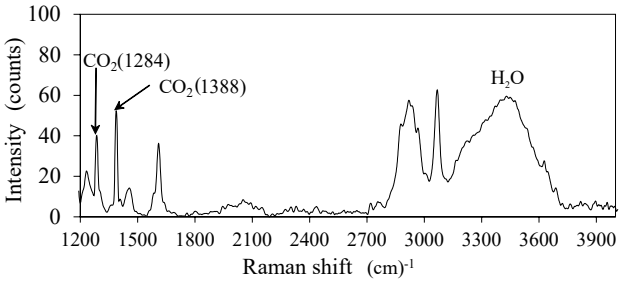

FIGURE 8. Raman spectrum of CO_2 bearing inclusions in quartz veins of the Daralu deposit (main stage: type-III).

The $(La/Yb)_n$ vs. $(Yb)_n$ diagram of numerical batch-melting modeling (Drummond *et al*., 1996) indicates that the Daralu adakitic-like porphyry can be derived by >10% melting of the heavy minerals source (*e.g.* garnet and amphibolite; Rapp *et al.*, 1991) and lack of plagioclase residual phase (Fig. 10).

The REEs patterns show strongly fractionated La_n/Yb_n (avg. of 28.73) in the chondrite normalized plot (Fig. 11A). High chondrite-normalized La/Sm and Dy/Yb ratios can show enrichment of amphibole and garnet as residual phases in melt source for the Daralu porphyry. Also, lack of negative Eu anomalies ($Eu_n/Eu^* \approx 1$) and LREEs enrichments, but flat to concave-downward MREEs-HREEs patterns, reflected in $[Dy/Yb]_n$= 0.71–2.22 and $[La/Sm]_n$= 4.81–15.27 can provide evidence supporting the amphibole involvement with minor garnet as a residual phase in the melt source.

These samples were depleted in Nb, Ta, Th, Zr, Hf and Ti as High-Field Strength Elements (HFSEs) and enriched in Cs, Rb, Ba and Pb as Large-Ion Lithophile Elements (LILEs) in primitive mantel-normalized spider plot (Fig. 11B).

The high values of LREEs indicate enrichment of mobile elements in magma during the dehydration process in melting temperature of the magma source (Rollinson, 1993) and thus confirm the hydration of these magmas. However, the low values of Yb indicate the presence of garnet and amphibole in the residual magma due to the preferential entrance of HREEs in these minerals (Yan Wang *et al*., 2007). The distinct negative HFSEs anomalies (*e.g.* Ta, Nb and Ti) of the Daralu porphyry also suggest that the source rocks could have melted under high pressure (≥15Kbars) physical status (Xiong *et al.*, 2006) in the

TABLE 4. Comparison of Daralu stock geochemical features with an adakitic magma

	SiO_2 (wt.%)	Na_2O (wt.%)	Al_2O_3 (wt.%)	K_2O (wt.%)	MgO (wt.%)	Rb (ppm)	Yb (ppm)	Y (ppm)	Sr (ppm)	Sr/Y	Eu/Eu*	Zr/Sm	La/Yb
Adakite like rocks	>56	>3.5	> 15	<3	< 3	≤65	≤1.9	≤18	≥400	≥20	≥1 (No Eu negative anomaly)	>30	≥20
Daralu granitoid (average values)	62.48	4.38	15.56	2.74	1.36	50.53	0.66	6.46	400.77	78.01	1.35	52.31	37.31
Ref.	1	1	1	1	1	1	1	1	1	1	2	3	1

1. Richards and Kerrich, (2007), 2. Defant and Kepezhinskas (2001), and 3. Foley *et al.* (2002) and Eyuboglu *et al.* (2018)

presence of heavy minerals (Defant and Kepezhinskas, 2001). This evidence indicates that the KCMA formed in continental arcs with thickened crust during the Tertiary (Shafiei *et al.*, 2009).

The values of normalized LREEs/MREEs $([La/Sm]_n)$ and normalized MREEs/HREEs $([Dy/Yb]_n)$ ratios are reported in Table I, Appendix. All of the samples show moderate LREE enrichments ($[La/Sm]_n$= 4.81–15.27) but only weak enrichment of MREEs relative to HREEs ($[Dy/Yb]_n$= 0.71–2.22). According to Richards *et al.* (2012), these features can be used for discriminating the contribution of hornblende vs. garnet. The high $[Dy/Yb]_n$ values represent garnet fractionation and/or the presence of residual garnet in primary magmas, because as mentioned above, garnet has high partition coefficients for HREE.

The lack of negative europium anomaly (Table I, Appendix) in the Daralu is due to the fact that its source magma has originated from an environment in which plagioclase is not stable due to the presence of abundant water. Meanwhile, partial melting of plagioclase increases Eu and Sr in the remaining magma, which is typically pursued by formation of a productive magma (Kelemen *et al.*, 2003). The preferential fractionation

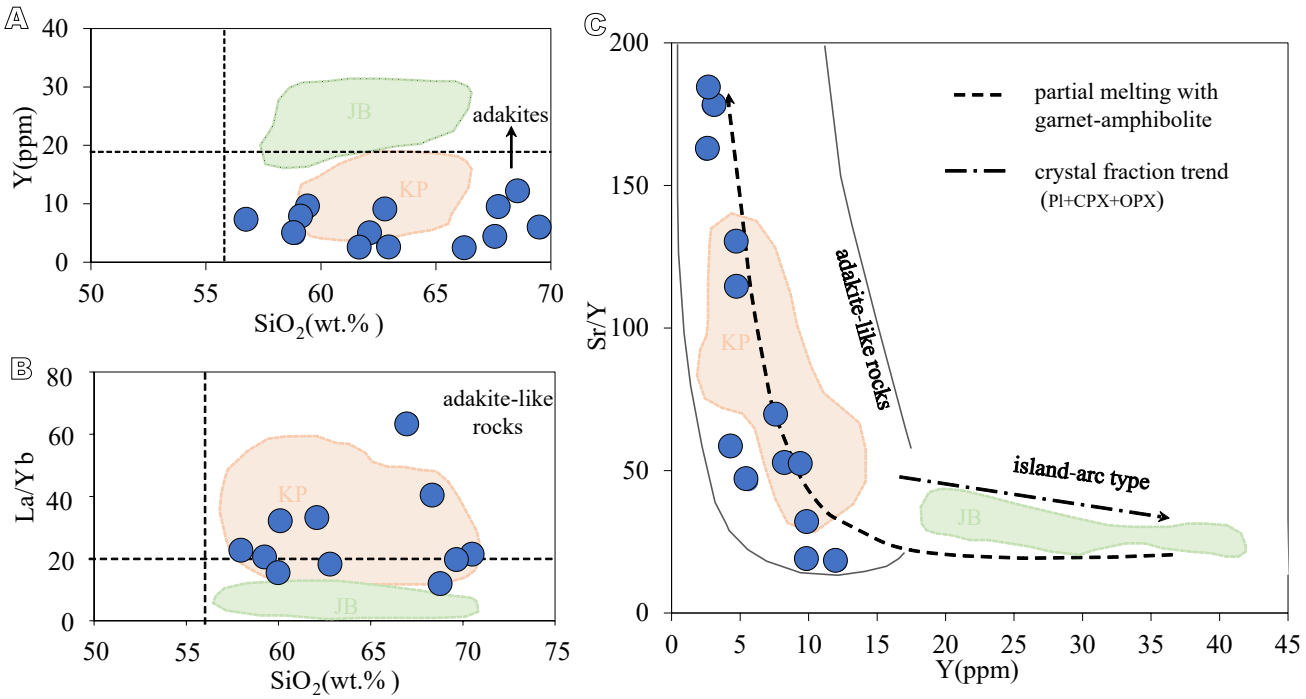

FIGURE 9. Plots of Daralu samples. A) Y vs. SiO_2 diagram (from Richards and Kerrich, 2007). B) La/Yb vs. SiO_2 diagram (from Richards *et al.*, 2012). C) Sr/Y vs. Y diagram (Defant and Drummond, 1990). Arrow (after Castillo, 2012) showing partial melting trend; and determining adakite-like field. The Kuh Panj (KP) and Jebal Barez (JB) fields in A are from Shafiei *et al.* (2009), and in B and C Asadi *et al.* (2014).

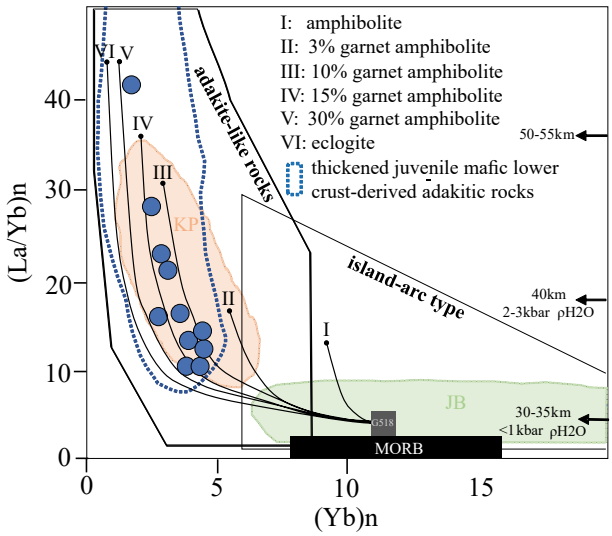

FIGURE 10. La/Yb vs. Yb (chondrite-normalized) diagram after Karsli *et al.* (2011). Data: adakite and island-arc fields are from Martin (1999). The G518 (Eastern Pontides gabbro) and MORB (Enriched-Mid oceanic Ridge Basalt) source rock are from Dokuz *et al.* (2006), and Sun and McDonough (1989), respectively. The simulated results of variable degrees of partial melting from Haschke *et al.* (2010). The field of thickened juvenile mafic lower crust-derived adakitic rocks is from Xiong *et al.* (2003). The KP and JB fields are from Asadi *et al.* (2014).

of hornblende than plagioclase accumulation for the europium anomaly increases in the productive porphyries (Richards *et al.*, 2012) such as Daralu porphyry system.

Geodynamic setting

The change of tectonic regime from pre- to post–collision between the Afro-Arabian and Eurasian plates in the KCMA led to transition from normal calc-alkaline arc magmatism in the Eocene–Oligocene (JB-type) to adakite-like magmatism (KP-type) in the mid–late Miocene–Pliocene (Asadi *et al.*, 2014; Richards *et al.*, 2012; Shafiei *et al.*, 2009). This is attributed to transpressive crustal shortening and thickening (Asadi *et al.*, 2014; Shafiei *et al.*, 2009). In several previous regional studies of the KCMA, there are possible links between adakite-like porphyry and mineralization (Aghazadeh *et al.*, 2015; Asadi, 2018; Atapour and Aftabi, 2021; Zarasvandi *et al.*, 2019).

Several scenarios have already been proposed for the development of adakitic or adakitic-like melts: i) melting of the thickened continental crust at arc or post-collision continental crusts (*e.g.* Topuz *et al.*, 2011); ii) partial melting of subducted basaltic oceanic slab (*e.g.* Defant and Derummond, 1990; Delavari *et al.*, 2014); iii) low-grade melting of the metasomatized mantle (*e.g.* Gao *et al.*, 2007) and iv) high-pressure crystallization with garnet partnership (*e.g.* Macpherson *et al.*, 2006).

In the case of the Daralu deposit, the adakitic-like feature is explained by high thickness of the continental crust and melting equilibrium at pressures greater than 10kb and outside the stability range of stable plagioclase, similar to the adakitic-like melts of active continental margins with high thickness (Topuz *et al.*, 2011). Asadi *et al.* (2014) proposed a petrogenetic model based on partial melting of a mafic lower crust for the adakitic melts of the KP granitoids of the KCMA. Referring to the diagram of Figure 9C, the Daralu samples show similar partial melting trend (dashed line).

The Daralu samples plotted on the Th/Yb vs. La/Yb diagram (Condie, 1989; Fig. 12A) show the tectonic setting of continental arc margin within high arc maturity. In addition, as shown in Figure 12B, the tectonic setting of the Daralu deposit is mainly post-collisional within the normal continental arc in the R_1–R_2 diagram (R_1=4Si–11[Na+K]-2[Fe+Ti] vs. R_2=6Ca+2Mg+Al) (De la Roche *et al.*, 1980).

This environment in the KCMA is consistent with the Alpine-Himalayan collision and crustal thickening arising from magmatic arc evolution. The Neo-Tethys Ocean was closed at early Cenozoic (Dargahi *et al.*, 2010)

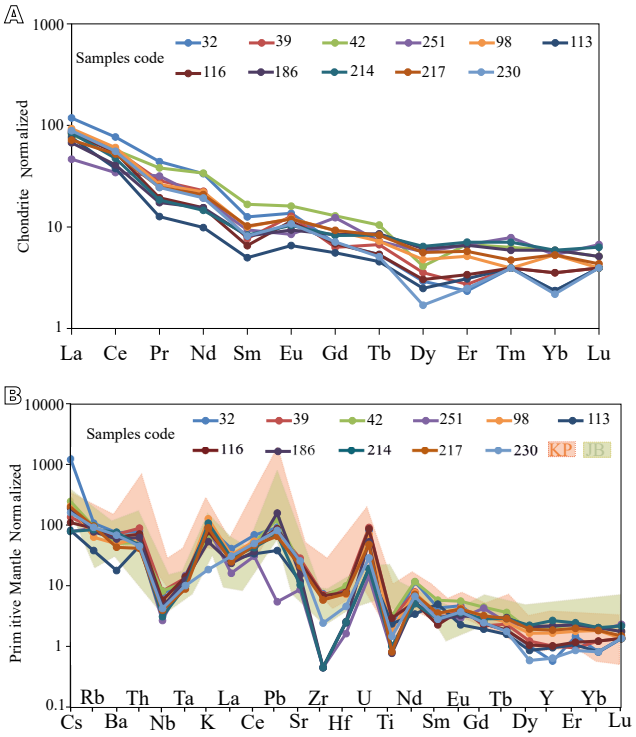

FIGURE 11. Spider diagrams. A) REE normalized by chondrite (Sun and McDonough, 1989). B) Multi-element normalized by primitive mantle (Sun and McDonough, 1989). The KP and JB data are from Shafiei *et al.* (2009).

and the subsequent collisional orogeny occurred during the tectonic evolution. The dating results confirm that the Daralu porphyry deposit with middle Miocene age (12.96Ma; Aghazadeh *et al.*, 2015) is associated with the subsequent collisional regime.

According to Xiao and Clemens (2007), partial melting of mafic rocks at pressures equivalent to 40–50km crustal thickness (1.2–1.5GPa) can lead to the generation of adakitic melts. The La/Yb ratio content can be a proxy for the crustal thickness (Profeta *et al.*, 2015). This ratio for the analyzed samples indicates a probable 40–55km crustal thickness in the Daralu suite (Fig. 13A). Lack of Ni and MgO contents in the adakitic magma from the thickened lower continental crust is due to the fact that magma does not pass through the mantle wedge. The Daralu samples have low Mg# numbers (<41.90) and MgO content (<2.77wt.%); therefore, they are plotted in the field of adakitic rocks formed by melting of the thickened lower crust (Figs. 13B; 14B), which is consistent with the Eocene adakitic magmas formed by the Central Iranian crust melting with thickness of >40km (Rapp *et al.*, 2002). Moreover, the samples with relatively high K_2O are in the range of adakite in the Fe_2O_3–K_2O–MgO ternary diagram (Aguillón-Robles *et al.*, 2001; Fig. 14A); therefore, it can be concluded that the source materials of the Daralu intrusive body originated from lower thickened crust, where the garnet-bearing amphibolitic materials contain relatively high K_2O (Fig. 14C, D).

Fluid evolution

The fluid evolution derived from fluid compositions and P–T evaluations shows an initial trend of decreasing pressure and salinity, further fluid cooling and boiling, and mixing with meteoric water, leading to sulfide precipitation in the Daralu deposit.

The spatial and temporal relationships between quartz veins and mineralization in the Daralu PCD, and the occurrence of various types of FIs (Table 3) indicate that the early forming and the main metallogenic fluid was derived from relatively CO_2-rich to CO_2-poor aqueous phases due to the input of meteoric fluids. The values of Te (Ice) offer various amounts of cations Na^+, K^+, Ca^{2+}, Mg^{2+} and Fe^{2+} in the type II FIs (Shepherd *et al.*, 1985).

The T_h of fluid inclusions decreased from 451–580ºC during the early ore-forming stage, to 217–395ºC in the main stage, and finally to 210–310ºC in the late stage. The FIs salinities evolved from 7.9–21.7wt.% NaCl eqv. in the early stage, with two clusters 3–12.2 and 35.9–55.9wt.% NaCl eqv. in the main stage, and 5.7–18.9wt.% NaCl eqv. in the late stage. The FIs salinities in the main ore stage are clearly higher than in the early and late ore stages, and show two different clusters (Fig. 15), which can be interpreted by escape of volatile phases (brine-vapor boiling) and fluid immiscibility (*e.g.* Dugdale and Hagemann, 2001; Hao *et al.*, 2015).

As shown in Figure 15, the temperature of fluids in the Daralu deposit decreases from the early stage to the final stage, whereas salinity increases from the early stage to the main stage, and then decreases in the final stage. This indicates the primary magmatic origin of the mineralized fluids, subsequent development of the hydraulic fractures, and mixture of primary magmatic fluids with the meteoric fluids. These occurrences are responsible for the evolution of hydrothermal system towards low temperatures and salinity (Canet *et al.*, 2011). The events such as NaCl supersaturation, exhaustion of CO_2-rich components during hydrothermal system evolution in the primitive fluids, high oxygen fugacity (based on the aqueous inclusions containing hematite), and temperature decreasing through mineralization stages could be observed in the PCDs

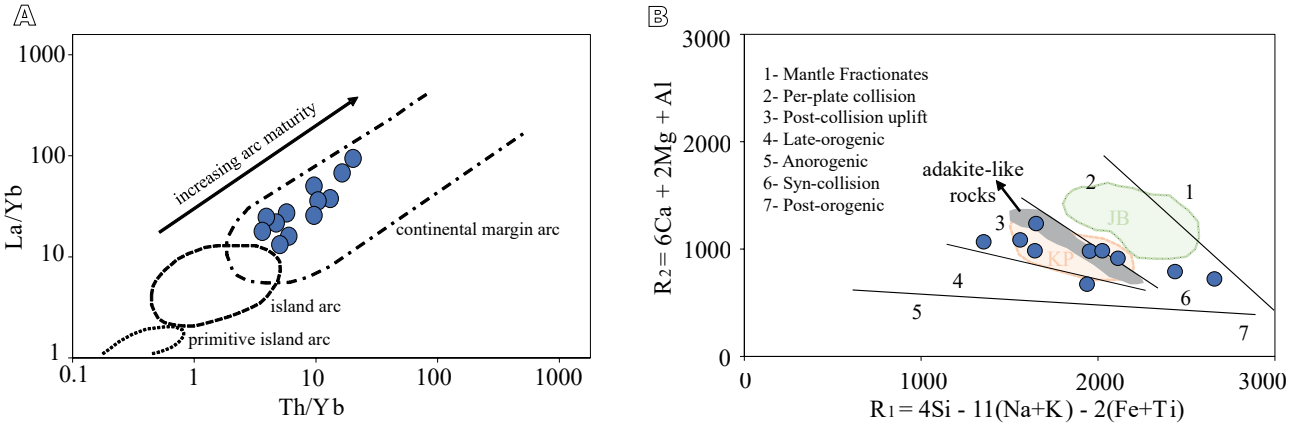

FIGURE 12. Geochemical correlation plots. A) La/Yb vs. Th/Yb from Condie (1989). B) R1 vs. R2 after Batchelor and Bowden (1985). The Daralu granitoid porphyry samples are mainly located in the post-collision uplift field. Adakite-like field (gray color) after Karsli *et al.* (2011) and the KP and JB fields after Asadi *et al.* (2014).

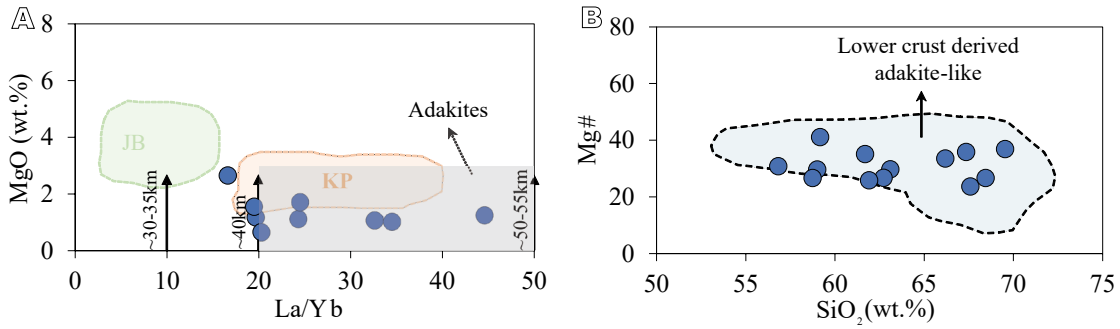

FIGURE 13. Plots of Daralu samples. A) MgO vs. La/Yb diagrame. The crustal thickness data after Ahmadian *et al.* (2009). Fields reference: adakites field from Richards and Kerrich (2007), and KP and JB fields after Shafiei *et al.* (2009). B) Mg# [(Mg numbers= 100×MgO/(MgO+0.9FeOtot)] vs. SiO_2 diagram. The thick lower crust derived adakite-like field based on Wang *et al.* (2006).

repressing anomalously high mineralization (Pirajno, 2009).

The microthermometric results of this study showed that the FIs containing halite crystals in early veins were dominantly homogenized with halite melting. This feature is compatible with the behavior of halite-saturated FIs in economic porphyry systems (Bouzari and Clark, 2006). This compatibility could be attributed to supersaturation of halite before trapping or inhomogeneous trapping of halite-saturated fluids. These supersaturated fluids that are the sources of copper-bearing minerals tolerate the boiling process (Rusk *et al.*, 2008). The coexistence of multiphase with vapor-rich FIs may display immiscibility or boiling during the trapping of these fluids.

The occurrence of CO_2-bearing FIs has been reported in porphyry systems that are related to collision settings (Li *et al.*, 2007). The presence of CO_2 in the melts would result in early and deep magma degassing (Wallace, 2005). Significantly, removal of CO_2 from the system can be considered as a reducing factor which can play a main

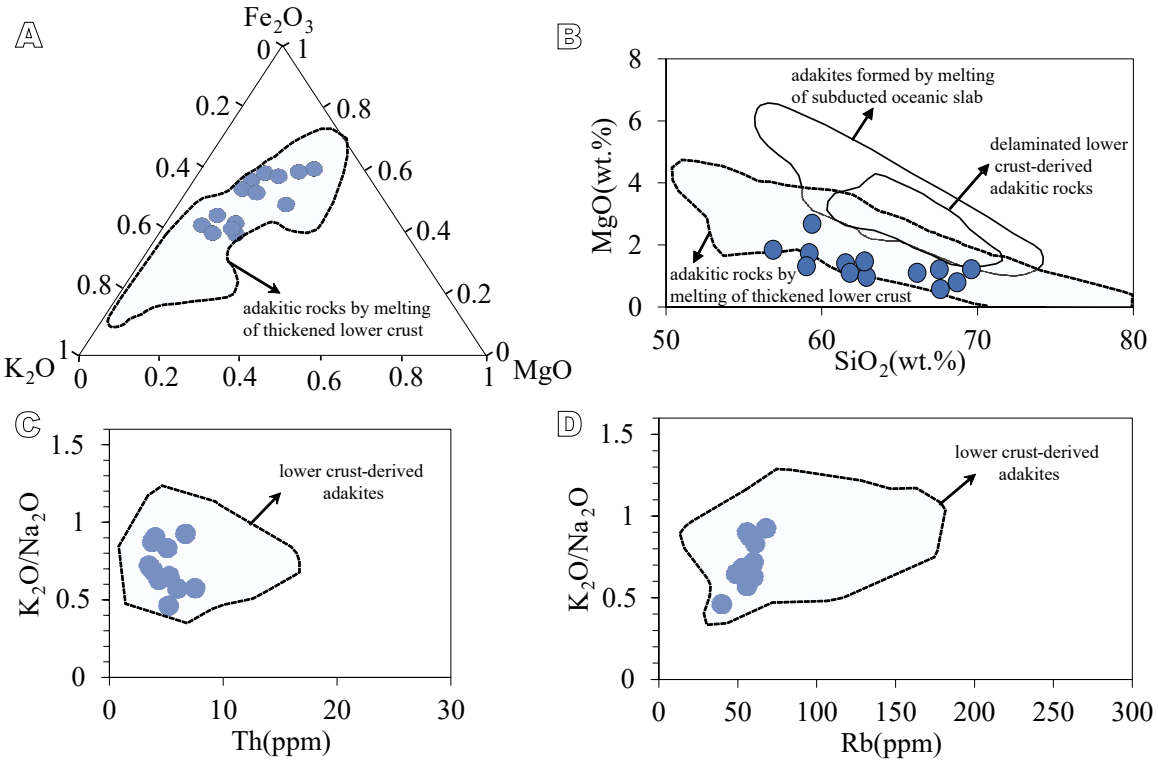

FIGURE 14. A) Fe_2O_3–K_2O–MgO ternary diagram. B) SiO_2 vs. MgO diagram, designated fields are from Karsli *et al.* (2011) and references therein. C) K_2O/Na_2O vs. Th. D) K_2O/Na_2O vs. Rb. C and D diagrams after Delavari *et al.* (2014), indicating that the Daralu rocks generated by partial melting of thickened mafic lower crust.

role in the abundances of metals, and thus promoting the mineralization (Liang *et al.*, 2009). This is due to the transported metal complexes and sulfur in the reduction conditions and stability of complexes until the final stages of mineralization (Pokrovski *et al.*, 2008). The main ore–forming stage of copper occurred by advanced H_2O+CO_2 boiling and subsequent early–stage cooling of ore-forming fluid in the Daralu PCD.

The trapping pressures of H_2O–CO_2–NaCl system, measured by the FLUIDS software (Bakker, 2003), were between 145 to 980MPa, which is equivalent to depths between 3.6 and 5.3 kilometers (assuming ~27MPa per 1km of pressure gradient). These depths coincide with the 1–5km mineralization depth of porphyry deposits (Pirajno, 2009). The decrease in trapping pressure of the fluid inclusions is like the Alpine–Himalayan magmatic–hydrothermal systems (Li *et al.*, 2012).

According to Table 3, in the late-stage, the pressure decreases with salinity and temperature, showing fluids dilution and cooling during the late stage. Kreuzer (2005) proposed that events such as the decrease in pressure, temperature and salinity from early toward late stages can be attributed to the mixing process of hydrothermal fluid with meteoric water. It is concluded that the fluid system evolution followed by input of meteoric water considerably reduces the salinity and temperature of magmatic fluid in the Daralu PCD.

The magmatic-hydrothermal fluids of porphyry systems that originated from lower thickened juvenile continental crust in collisional settings, show relatively high CO_2/H_2O ratios (Yang *et al.*, 2013). Asadi *et al.* (2013) and Zarasvandi *et al.* (2019) suggested that the CO_2-bearing fluid inclusions could be the indicative markers for porphyry systems in collisional settings. Therefore, it is suggested that the moderate activity of NaCl as a result of high CO_2 content in ore-forming fluids (Robb, 2005), and the increase of H_2S/HS activity (S_2^-) due to the CO_2 effervescence (Asadi, *et al.*, 2013) possibly lead to precipitation of chalcopyrite and other sulfide minerals in the Daralu porphyry system.

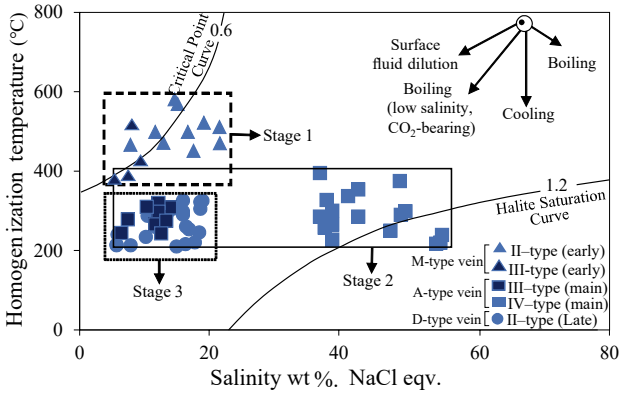

FIGURE 15. Diagram of homogenization temperature vs. salinity for 70 fluid inclusions in quartz from three different quartz veins (M-type, A-type and D-type) of the Daralu PCD. The critical point and halite saturation curves showing densities (g/cm^{-3}) of fluid inclusions (after Wilkinson, 2001). Daralu hydrothermal fluid evolution is mainly controlled by decreasing in homogenization temperature and salinity trend from stages 1 to 3. Evolutionary paths (Surface fluid dilution, Boiling [low salinity, CO_2–bearing], Cooling and Boiling) after Wilkinson (2001).

The sulfur isotope data of pyrite and chalcopyrite of all types of veins in the Daralu porphyry system show an average of $\delta^{34}S$= 5.5‰ (Table 2) which is close to the values analyzed for other KP-type deposits in the KCMA central part such as; $\delta^{34}S$= 2.4‰ for Dareh Zar (Aghazadeh *et al.*, 2015), $\delta^{34}S$= 0.9‰ for Sarcheshmeh (McInnes *et al.*, 2003), and $\delta^{34}S$= 2.7‰ for Sarkuh (Mirnejad *et al.*, 2013). This feature of the Daralu deposit complies with values analyzed for granitic rocks (Hoefs, 2009), and is similar to many porphyry systems with an average range of 0 to 5‰, which confirms their magmatic origin (Shanks, 2014).

Sulfur isotope composition in magmatic-hydrothermal systems is determined by factors such as temperature, pH and oxygen fugacity (fO_2), the total sulfur isotopic composition of fluid ($\Sigma\delta^{34}S$), and the oxidized sulfur species versus reduced species (SO_4/H_2S ratio) of hydrothermal fluid (Ohmoto and Ray, 1979). High values of ^{34}S may be related to the interaction between the magmatic sulfur and an enriched source of ^{34}S (evaporative units) and/or the wall rock assimilation (Hoefs, 2009) or may be related to the dissolution and mobility of pre-deposited ores. No high evaporation and sedimentary sulfides with heavier isotope composition of sulfur have been reported from the Daralu area.

Wagner *et al.* (2004) and Li *et al.* (2012) proposed that magmas with high CO_2 content have undergone significant amounts of crustal fusion, which are observed typically in intercontinental hydrothermal systems such as porphyry, skarn, and Iron Oxide Copper-Gold (IOCG) deposits. Since CO_2 was detected in the FIs of the Daralu deposit, it is suggested that the parent magma of this porphyry was significantly impregnated with the crustal material. Taghipour (2007) indicated that the fluids of relatively oxidized I-type granitoids will tend to be $\delta^{34}S$ ~4‰ more enriched than their source magma.

Implications for economic potential

The main aspects of a productive porphyry are MnO <0.1wt.%, Y <18ppm, and the concentrations of <100ppm for HFSEs (Lang and Titley, 1998). Accordingly, the Daralu samples are plotted on the productive field of the Y vs. MnO diagram (Fig. 16A).

The positive anomaly of europium observed in the Daralu deposit (Fig. 16B) can be attributed to the availability of large amounts of water and high oxygen fugacity in the lower crustal sources of magma (Richards *et al.*, 2012), leading to an oxidative hydrous magma. The magmas formed under oxidant conditions can result in the separation of sulfide phases and carrying the sulfur and copper to the final stages of crystallization, which eventually can give rise to the porphyry copper mineralization (Mungall, 2002).

The connection between adakitic stocks and the PCDs has already been suggested by some authors (*e.g.* Conly *et al.*, 2006; Hattori and Keith, 2001; Richards and Kerrich, 2007). In the UDMA, most of the economic PCDs (Kuh Panj-type) are associated with adakitic intrusions (Asadi *et al.*, 2014). Hollings *et al.* (2005) stated that only those adakites that are formed by melting of the lower mafic crust or by the fractional crystallization of the hydrous basaltic magmas contain the key factors for Cu mineralization. Dehydration of magma during its evolution is a dominant factor that leads to entrance of chalcophile elements (*e.g.* Cu and Mo) into the adakitic magmas (Liu *et al.*, 2010).

The fluid inclusion data of the Daralu porphyry including NaCl supersaturation, CO_2 presence in the ore-forming fluids, temperature decrease in the main stage of mineralization with signs of boiling, and high oxygen fugacity (presence of hematite) suggest that the mineralization potential has increased during the evolution of a hydrothermal system.

According to the microthermometric data in quartz veins, the fluid system evolved from high-temperature, medium-salinity, high-pressure and CO_2-rich to low-temperature, low-pressure, high-salinity and CO_2-poor, with fluid boiling being the dominating mechanism, followed by input of meteoric water. The scape of CO_2 may have been a factor in increasing the activities of NaCl in the fluids, diminishing the oxidation of the fluids from stage 1 to 3. The result was precipitation of sulfides and trapping of multi–phase solid inclusions in hydrothermal quartz veins.

CONCLUSIONS

Based on geochemical data, the Daralu system is a highly mineralized economic PCD. Evaluating the attributes of the magmatic-hydrothermal systems and its progress from early to main, and late stages, led us to a better understanding of fertility signatures in the Daralu collisional PCD. The key signatures could be predicted by the following conclusions:

i) Similar to other productive porphyry granitoids of KP-type in the KCMA, the Daralu porphyry intrusive is a peraluminous I-type granodiorite with high-K calc-alkaline nature that shows adakitic-like affinity by high Sr, and low Y and Yb. These features, along with the high LREE, low HREE, and absence of europium anomaly, indicate that the Daralu magmatic suite has originated from a hydrous-oxidant magma with the plagioclase-free environment in which the amphibole and garnet play the main role of REE distribution/separation in the residual melting.

ii) The Daralu deposit is characterized by negative anomalies of Nb, Ti, and Ta, and high Sm/Yb values, representing the high assimilation of a thickened crust which indicates the garnet contribution in a high-pressure condition during the evolution of Daralu intrusion. This deposit was formed in a post-collisional tectonic setting and can be considered as one of the Miocene intrusions of the UDMA.

iii) La/Sm and Sm/Yb ratios of the Daralu samples show an increasing trend of the crustal thickening similar to the Andean orogenic belt which is also confirmed by the La/Yb ratio that presumably indicates 40–55km crustal thickness in the Daralu suite. Based on this evidence and the Mg number (Mg#), we concluded that Daralu adakitic magma was originated from melting of a thickened mafic lower crust.

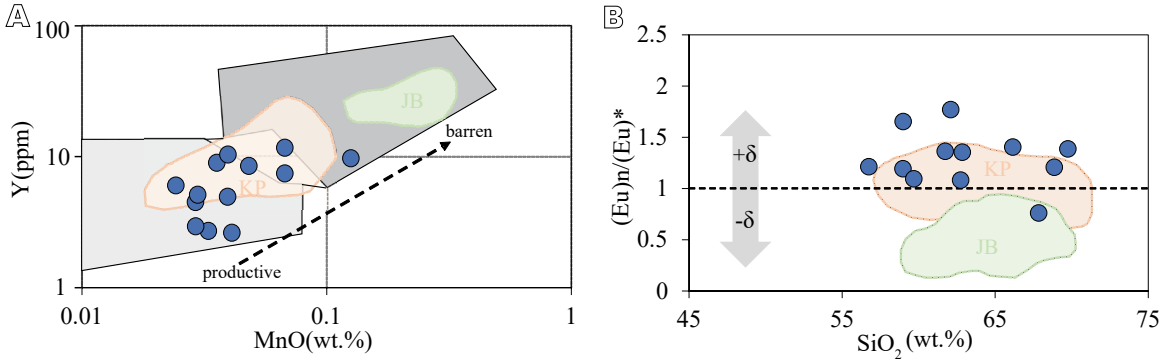

FIGURE 16. Plots of A) MnO vs. Y, after Baldwin and Pearce (1982). B) Eu_n/Eu^* ($Eu^*= \sqrt{Sm_n + Gd_n}$) vs SiO_2, based on Richards *et al.* (2001), diagrams in comparison with hydrous-oxidized productive and barren porphyry granitoid rocks of KCMA after Asadi *et al.* (2014).

iv) Homogenization temperature decreases and salinity of fluid inclusions increases from the pre- to main ore stages during hydrothermal fluid evolution. Most of the fluid inclusions in the primitive hydrothermal fluids represented NaCl supersaturation (35.98–55.95wt.% NaCl eqv.) in the Daralu deposit. CO_2 is present in the fluid inclusions of early-stage and losses in the late stage during magmatic-hydrothermal transition. The hematite and magnetite occurrence in fluid inclusions of the pre-ore stage indicated high oxygen fugacity and is of critical importance for sulphate reduction and copper mineralization. Integration of these factors indicates a magmatic-hydrothermal fluid favor with high contents of metal and sulfur for generation of an economic deposit in the Daralu area.

v) The positive content of $\delta^{34}S$ (avg. +5.5‰) at the Daralu deposit can be described by the contribution originating from crustal sources through the sulfurization process.

vi) In contrast to the previous arguments (*e.g.* Asadi *et al.*, 2014; Khosravi *et al.*, 2019; Shafiei *et al.*, 2009; Zarasvandi *et al.*, 2015), geochemical data of this work suggested that Daralu is associated with an adakitic intrusion originating from partial melting of a garnet-bearing mafic source of thickened lower crust in a collisional setting.

v) Based on the results presented here, the intimate relationship between the adakitic magmas and fertile metallogenic environment, as well as orogenic arc crust evolution for porphyry deposits in the economic KP type, the Daralu could be considered as an economic PCD. It can be explained by high Cu grade (~0.4%) and tonnage (~200Mt) data in the Daralu.

ACKNOWLEDGMENTS

The Research and Development Center of National Iranian Copper Industries Company (NICICo) funded this work. Authors are sincerely grateful to the Daralu mine staff for providing the facilities during field works.

REFERENCES

Afshooni, S.Z., Mirnejad, H., Esmaeily, D., Haroni, H.A., 2013. Mineral chemistry of hydrothermal biotite from the Kahang porphyry copper deposit (NE Isfahan), Central Province of Iran. Ore Geology Reviews, 54, 214-232.

Aghazadeh, M., Hou, Z., Badrzadeh, Z., Zhou, L., 2015. Temporal-spatial distribution and tectonic setting of porphyry copper deposits in Iran: Constraints from zircon U–Pb and molybdenite Re-Os geochronology. Ore Geology Reviews, 70, 385-406. DOI: http://dx.doi.org/10.1016/j.oregeorev.2015.03.003

Aguillón-Robles, A., Caimus, T., Bellon, H., Maury, R.C., Cotton, J., Bourgois, J., Michaud, F., 2001. Late Miocene adakites and Nb-enriched basalts from Vizcaino Peninsula, Mexico: indicators of East Pacific Rise subduction below southern Baja California. Geology, 29, 531-534.

Ahmad, T., Posht Kuhi, M., 1993. Geochemisty and petrogenesis of Urumiah-Dokhtar volcanics around Nain and Rafsanjan areas: a preliminary study. In: Ahmad, T., Posht Kuhi, M. (eds.). Geochemistry and petrogenesis of Urumiah–Dokhtar volcanic belt around Nain and Rafsanjan area; Miner Depositaa preliminary study: treatise on the geology of Iran. Iranian Ministry of Mines and Metals, 90pp.

Ahmadian, J., Haschke, M., McDonald, I., Regelous, M., Ghorbani, M.R., Emami, M., Murata, M., 2009. High magmatic flux during Alpine–Himalayan collision: Constraints from the Kal-e-Kafi complex, Central Iran. Geological Society of America Bulletin, 121, 857-868. DOI: http://dx.doi.org/10.1130/B26279.1

Alavi, M., 2004. Regional stratigraphy of the Zagros fold-thrust belt of Iran and its proforeland evolution. American Journal of Science, 304, 1-20.

Asadi, S., 2018. Trigers for the generation of post-collisional porphyry Cu systems in the Kerman magmatic copper belt, Iran: new constraints from elemental and isotopic (Sr-Nd-Hf-O) data. Gondwana Research, 64, 97-121. DOI: https://doi.org/10.1016/j.gr.2018.06.008

Asadi, S., Moore, F., Fattahi, N., 2013a. Fluid inclusion and stable isotope constraints on the genesis of the Jian copper deposit, Sanandaj–Sirjan metamorphic zone, Iran. Geofluids, 13, 66-81.

Asadi, S., Moore, F., Zarasvandi, A., Khosrojerdi, M., 2013b. First report on the occurrence of CO2-bearing fluid inclusions in the Meiduk porphyry copper deposit, Iran: implications for mineralization processes in a continental collision setting. Geologos, 19, 301-320. DOI: http://dx.doi.org/10.2478/logos–2013–0019

Asadi, S., Moore, F., Zarasvandi, A., 2014. Discriminating productive and barren porphyry copper deposits in the southeastern part of the central Iranian volcano-plutonic belt, Kerman region, Iran: A review. Earth-Science Reviews, 138, 25-46. DOI: https://doi.org/10.1016/j.earscirev.2014.08.001

Atapour, H., 2007. Geochemical Evolution and Metallogeny of Potassic Igneous Rocks of the Volcano-plutonic Belt of Kerman Province with Particular Reference to Special Elements. Ph.D. Thesis. Kerman (Iran), Shahid Bahonar University, 401pp.

Atapour, H., 2017. The exploration signifcance of Ag/Au, Au/Cu, Cu/Mo, (Ag×Au)/(Cu×Mo) ratios, supra-ore and sub-ore halos and fluid inclusions in porphyry deposits: a review. Islamic Republic of Iran, Journal of Sciences, 28, 133-146.

Atapour, H., Aftabi, A., 2021. Petrogeochemical evolution of calcalkaline, shoshonitic and adakitic magmatism associated with Kerman Cenozoic arc porphyry copper mineralization, southeastern Iran: A review. Lithos, 398-399, 106261. DOI: http://dx.doi.org/10.1016/j.lithos.2021.106261

Bakker, R.J., 2003. Package FLUIDS 1. Computer programs for analysis of fluid inclusion data and for modelling bulk fluid properties. Chemical Geology, 194, 3-23.

Batchelor, R.A., Bowden, P., 1985. Petrogenetic interpretation of granitoid rock series: using multinational parameters. Chemical Geology, 48, 43-55.

Berberian, F., Muir, I.D., Pankhurst, R.J., Berberian, M., 1982. Late Cretaceous and early Miocene Andean type plutonic activity in northern Makran and Central Iran. Journal of the Geological Society of London, 139, 605-614.

Bodnar, R.J., 1993. Revised equation and table for determining the freezing point depression of H2O-NaCl solutions. Geochimica et Cosmochimica Acta, 57, 683-684.

Bodnar, R.J., 1995. Fluid inclusion evidence for a magmatic source for metals in porphyry copper deposits. Mineralogical Association of Canada Short Course Series, 23, 139-152.

Bodnar, R.J., Lecumberri-Sanchez, P., Moncada, D., Steele-MacInnis, M., 2014. Fluid inclusions in hydrothermal ore deposits. In: Holland, H.D., Turekian, K.K. (eds.). Treatise on geochemistry. Oxford, Elsevier, 119-142.

Bouzari, F., Clark, A.H., 2006. Prograde evolution and geothermal affinities of a major porphyry copper deposit: the Cerro Colorado hypogene protore, I Región, northern Chile. Economic Geology, 101, 95-134. DOI: https://doi.org/10.2113/gsecongeo.101.1.95

Bowers, T.S., Helgeson, H.C., 1983. Calculation of the thermodynamic and geochemical consequences of nonideal mixing in the system H_2O-CO_2-NaCl on phase relations in geologic systems: Equation of state for H_2O-CO_2-NaCl fluids at high pressures and temperatures. Geochimica et Cosmochimica Acta, 47, 1247-1275.

Burke, E.A.J., 2001. Raman microspectrometry of fluid inclusions. Lithos, 55, 139-158.

Canet, C., Franco, S.I., Prol-Ledesma, R.M., González-Partida, E., Villanueva-Estrada, R.E., 2011. A model of boiling for fluid inclusion studies: application to the Bolaños Ag-Au-Pb-Zn epithermal deposit, Western Mexico. Journal of Geochemical Exploration, 110, 118-125.

Castillo, P.R., 2012. Adakite petrogenesis. Lithos, 135, 304-316. DOI: http://dx.doi.org/10.1016/j.lithos.2011.09.013

Charter and IDRO, 1971. Geological Survey, Iran, Geological Maps Kerman, (Yugoslav Institutes), 1:100,000.

Collins, P.L.F., 1979. Gas hydrates in CO2-bearing fluid inclusions and the use of freezing data for estimation of salinity. Economic Geology, 74, 1435-1444.

Condie, K.C., 1989. Origin of the earth crust. Palaeogeography, Palaeoclimatology, Palaeoecology, 75, 57-81.

Conly, A.G., Beaudoin, G., Scott, S.D., 2006. Isotopic constraints on fluid evolution and precipitation mechanisms for the Boléo Cu-Co-Zn district. Mineralium Deposita, 41, 27-151.

Dargahi, S., Arvin, M., Pan, Y., Babaei, A., 2010. Petrogenesis of post-collisional A-type granitoids from the Urumieh-Dokhtar magmatic assemblage, Southwestern Kerman, Iran: constraints on the Arabian-Eurasian continental collision. Lithos, 115, 190-204. DOI: https://doi.org/10.1016/j.lithos.2009.12.002

De la Roche, H., Leterrier, J., Grandclaude, P., Marchal, M., 1980. A classification of volcanic and plutonic rocks using R1, R2-diagrams and major element analysis-its relationships with current nomenclature. Chemical Geology, 29, 183-210.

Defant, M.J., Drummond, M.S., 1990. Derivation of some modern arc magmas by melting of young subducted lithosphere. Nature, 347, 662-665.

Defant, M.J., Kepezhinskas, P., 2001. Adakites: a review of slab melting over the past decade and the case for a slab–melt component in arcs. EOS Transactions of the American Geophysical Union, 82, 65-69.

Delavari, M., Amini, S., Schmitt, A.K., McKeegan, K.D., Mark Harrison, T., 2014. U–Pb geochronology and geochemistry of Bibi-Maryam pluton, eastern Iran: Implication for the late stage of the tectonic evolution of the Sistan Ocean. Lithos, 200-201, 197–211.

Diamond, L.W., 2003. Terms and symbols used in fluid inclusion studies. Mineralogical Association of Canada Short Course Series, 32. Last accessed: October 2023. Website: https://www.researchgate.net/publication/276024987

Dokuz, A., Tanyolu, E., Genc, S., 2006. A mantle- and a lower crust-derived bimodal suite in the Yusufeli (Artvin) area, NE Turkey: trace element and REE evidence for subduction-related rift origin of Early Jurassic Demirkent intrusive complex. International Journal of Earth Sciences, 95, 370-394.

Drummond, M.S., Defant, M.J., Kepezhinskas, P.K., 1996. Petrogenesis of slab-derived trondhjemite-tonalite-dacite/adakite magmas. Transactions, Royal Society of Edinburgh (Earth Science), 87, 205-215.

Dugdale, A.L., Hagemann, S.G., 2001. The Bronzewing lode-gold deposit, Western Australia: P-T-X evidence for fluid immiscibility caused by cyclic decompression in gold-bearing quartz veins. Chemical Geology, 173, 59-90.

Ellis, R., 1991. Sar-Cheshmeh. Mining Magazine, October, 192-196.

Emmons, S.F., 1918. Principles of Economic Geology. New York, McGraw-Hill, 1st edition, 550pp.

Eyuboglu, Y., Dudas, F.O., Santosh, M., Gümrük, T.E., Akbulut, K., Yi, K., Chatterjee, N., 2018. The final pulse of the Early Cenozoic adakitic activity in the Eastern Pontides Orogenic Belt (NE Turkey): An integrated study on the nature of transition from adakitic to non-adakitic magmatism in a slab window setting. Journal of Asian Earth Sciences, 157, 141-165. DOI: https://doi.org/10.1016/j.jseaes.2017.07.004

Foley, S.F., Tiepolo, M., Vannucci, R., 2002. Growth of early continental crust controlled by melting of amphibolite in subduction zones. Nature, 417, 637-640.

Frezzotti, M.L., Tecce, F., Casagli, A., 2012. Raman spectroscopy for fluid inclusion analysis. Journal of Geochemical Exploration, 112, 1-20. DOI: https://doi.org/10.1016/j.gexplo.2011.09.009

Gao, Y., Hou, Z., Kamber, B., Wei, R., Meng, X., Zhao, R., 2007. Adakite-like porphyries from the southern Tibetan continental collision zones: evidence for slab melt metasomatism. Contributions to Mineralogy and Petrology, 153, 105-120. DOI: http://dx.doi.org/10.1007/s00410–006–0137–9

Ghasemi, A., Talbot, C.J., 2006. A new tectonic scenario for the Sanandaj-Sirjan zone (Iran). Journal of Asian Earth Sciences, 26, 683-693.

Guilbert, J.M., Park, C.F., 1986. The Geology of Ore Deposits. New York, W.H. Freeman, 985pp.

Habibi, T., Hezarkhani, A., 2012. Hydrothermal evolution of Daraloo porphyry copper deposit, Iran: Evidence from fluid inclusions. Arabian Journal of Geosciences, 6, 1945-1955.

Hall, D.L., Sterner, S.M., Bodnar, R.J., 1988. Freezing point depression of NaCl-KCl-H2O solutions. Economic Geology, 83, 197-202.

Hao, Y.J., Ren, Y.S., Yang, Q., Duan, M.X., Sun, Q., Fu, L.C., Li, C., 2015. Ore genesis and formation age of the Gaogangshan Mo deposit, Heilongjiang province, NE China. Resource Geology, 65, 177-192.

Harris, A.H., Golding, S.D., White, N.C., 2005. Bajo de la Alumbrera copper-gold deposit: stable isotope evidence for a porphyry-related hydrothermal system dominated by magmatic aqueous fluids. Economic Geology, 100, 863-886.

Haschke, M., Pearce, J.A., 2006. Lithochemical exploration tools revisited: MnO and REE. Mendoza (Argentina), GSA Abstracts with Programs, 2 (Special Meeting), 116pp.

Haschke, M., Ahmadian, J., Murata, M., McDonald, I., 2010. Copper mineralization prevented by arc-root delamination during Alpine-Himalayan collision in Central Iran. Economic Geology, 105, 855-865. DOI: https://doi.org/10.2113/gsecongeo.105.4.855

Hassanzadeh, J., 1993. Metallogenic and tectono-magmatic events in the SE sector of the Cenozoic active continental margin of Iran (Shahr-e-Babak area, Kerman province). Ph.D. Thesis. United States of America (USA), University of California, Unpublished, 204pp.

Hattori, K.H., Keith, J.D., 2001. Contribution of mafic melt to porphyry copper mineralization: evidence from Mount Pinatubo, Philippines, and Bingham Canyon, Utah, United States of America (USA). Mineralium Deposita, 36, 799-806.

Hedenquist, J.W., Richards, J.P., 1998. The influence of geochemical techniques on the development of genetic models for porphyry copper deposits. Reviews in Economic Geology, 10, 235-256.

Hezarkhani, A., Williams-Jones, A.E., 1998. Controls of alteration and mineralization in the Sungun porphyry copper deposit, Iran: evidence from fluid inclusions and stable isotopes. Economic Geology, 93, 651-670.

Hoefs, J., 2009. Stable Isotope Geochemistry. Springer, 286pp. DOI: 10.1007/978-3-540-70708-0

Hofmann, A.W., 1997. Mantle geochemistry; the message from oceanic volcanism. Nature, 385, 219-229.

Hollings, P., Cooke, D., Clark, A., 2005. Regional geochemistry of Tertiary igneous rocks in central Chile: implications for the geodynamic environment of giant porphyry copper and epithermal gold mineralization. Economic Geology, 100, 887-904.

Holloway, J.R., 1981. Composition and volumes of supercritical fluids in the Earth crust. In: Hollister, L.S., Crawford, M.L. (eds.). Fluid Inclusions: Applications to Petrology. Quebec, Mineralogical Association of Canada, 13-38.

Hosseini, M.R., Ghaderi, M., Alirezaei, S., Sun, W., 2017. Geological characteristics and geochronology of the Takht-e-Gonbad copper deposit, SE Iran: a variant of porphyry type deposits. Ore Geology Reviews, 86, 440-458.

Hosseinjani Zadeh, M., Tangestani, M.H., 2011. Mapping alteration minerals using sub-pixel unmixing of ASTER data in the Sarduiyeh area, southeastern Kerman Iran. International Journal of Digital Earth, 4(6), 487-504. DOI: https://doi.org/10.1080/17538947.2010.550937

Hou, Z.Q., Duan, L.F., Lu, Y.J., Zheng, Y.C., Zhu, D.C., Yang, Z.M., Yang, Z.S., Wang, B.D., Pei, Y.R., Zhao, Z.D., McCuaig, T.C., 2015. Lithospheric architecture of the Lhasa Terrane and its control on ore deposits in the Himalayan-Tibetan orogeny. Economic Geology, 110, 1541-1575. DOI: https://doi.org/10.2113/econgeo.110.6.1541

Irvine, T.N., Baragar, W.R.A., 1971. A guide to the chemical classification of the common volcanic rocks. Canadian Journal of Earth Sciences, 8, 523-548.

John, D.A., Ayuso, R.A., Barton, M.D., Blakely, R.J., Bodnar, R.J., Dilles, J.H., Gray, Floyd, Graybeal, F.T., Mars, J.C., McPhee, D.K., Seal, R.R., Taylor, R.D., Vikre, P.G., 2010. Porphyry copper deposit model, chap. B of Mineral deposit models for resource assessment. U.S. Geological Survey Scientific Investigations Report 2010–5070–B, 169pp.

Karsli, O., Ketenci, M., Uysal, I., Dokuz, A., Aydin, F., Chen, B., Kandemir, R., Wijbrans, J., 2011. Adakite-like granitoid porphyries in the Eastern Pontides, NE Turkey: potential parental melts and geodynamic implications. Lithos, 127, 354-372. DOI: https://doi.org/10.1016/j.lithos.2011.08.014

Kay, S.M., Mpodozis, C., 2001. Central Andes ore deposits linked to evolving shallow subduction systems and thickening crust. GSA Today, Geological Society of America, 11, 4-9.

Kelemen, P.B., Hanghoj, K., Green, A.R., 2003. One view of the geochemistry of subduction-related magmatic arcs, whit an emphasis on primitive andesite and lower crust. In: Rudnick, R.L., Holland, H.D., Turekian, K.K. (eds.). Treatise on Geochemistry. Elsevier, 3, 593-659. ISBN 0-08-043751-6

Khosravi, M., Rajabzadeh, M.A., Qinb, K., Asadid, H., 2019. Tectonic setting and mineralization potential of the Zefreh porphyry Cu-Mo deposit, central Iran: Constraints from petrographic and geochemical data. Journal of Geochemical Exploration, 199, 1-15.

Kreuzer, O.P., 2005. Intrusion-hosted mineralization in the Charters Towers goldfield, north Queensland: new isotopic and fluid inclusion constraints on the timing and origin of the auriferous veins. Economic Geology, 100, 1583-1603.

Lang, J.R., Titley, S.R., 1998. Isotopic and geochemical characteristics of Laramide magmatic system in Arizona and implications for the genesis of porphyry copper deposits. Economic Geology, 93, 138-170.

Li, N., Chen, Y.J., Zhang, H., Zhao, T.P., Deng, X.H., Wang, Y., Ni, Z.Y., 2007. Molybdenum deposits in East Qinling. Frontiers in Earth Sciences, 14, 186-198.

Li, N., Ulrich, T., Chen, U.J., Thomsen, T.B., Pease, V., Pirajno, F., 2012. Fluid evolution of the Yuchiling porphyry Mo deposit, East Qinling, China. Ore Geology Reviews, 48, 442-459.

Liang, H.Y., Sun, W.D., Su, W.C., Zartman, R.E., 2009. Porphyry copper-gold mineralization at Yulong, China, promoted by decreasing redox potential during magnetite alteration. Economic Geology, 104, 587-596.

Liu, Y.S., Gao, S., Hu, Z.C., Gao, C.G., Zong, K.Q., Wang, D.B., 2010. Continental and oceanic crust recycling-induced melt-peridotite interactions in the Trans-North China Orogen: U–Pb dating, Hf isotopes and trace elements in zircons from mantle xenoliths. Journal of Petrology, 51, 537-571.

Macpherson, C.G., Dreher, S.T., Thirwall, M.F., 2006. Adakites without slab melting: high pressure differentiation of island arc magma, Mindanao, the Philippines. Earth Planetary Science Letters, 243, 581-593.

Maniar, P.D., Piccoli, P.M., 1989. Tectonic discrimination of granitoids. Geological Society of America Bulletin, 101, 635-643.

Mao, J., Pirajno, F., Lehmann, B., Luo, M., Berzina, A., 2014. Distribution of porphyry deposits in the Eurasian continent and their corresponding tectonic settings. Journal of Asian Earth Sciences, 79, 576-584.

Martin, H., 1999. Adakitic magmas: modern analogues of Archaean granitoids. Lithos, 46, 411-429. DOI: https://doi.org/10.1016/S0024–4937(98)00076–0

Martin, H., Smith, R.H., Rapp, R., Moyen, J.F., Champion, D., 2005. An overview of adakite, tonalite trondhjemite-granodiorite (TTG), and sanitoid: relationships and some implications for crustal evolution. Lithos, 79, 1-24.

McClay, K.R., Whitehouse, P.S., Dooley, T., Richards, M., 2004. 3D evolution of fold and thrust belts formed by oblique convergence. Marine and Petroleum Geology, 21, 857-877.

McInnes, B.I.A., Evans, N.J., Belousova, E., Griffin, W.L., 2003. Porphyry copper deposits of the Kerman belt, Iran: timing of mineralization and exhumation processes. Scientific Research and Reports, Melbourne, Commonwealth Scientific and Industrial Research Organisation, 41pp.

McInnes, B.I.A., Evans, N.J., Fu, F.Q., Garwin, S., Belousova, E., Griffin, W.L., Bertens, A., Sukama, D., Permanadewi, S., Andrew, R.L., Deckart, K., 2005. Thermal history analysis of selected Chilean, Indonesian, and Iranian porphyry Cu-Mo-Au deposits. In: Porter, T.M. (ed.). Super Porphyry Copper and Gold Deposits: A Global Perspective. Adelaide, PGC publishing, 1-16.

Middlemost, E.A.K., 1994. Naming materials in the magma/igneous rock system. Earth-Science Reviews, 37, 215-224.

Mirnejad, H., Mathur, R., Hassanzadeh, J., Shafie, B., Nourali, S., 2013. Linking Cu mineralization to host porphyry emplacement: Re-Os ages of molybdenites versus U–Pb ages of zircons and sulfur isotope compositions of pyrite and chalcopyrite from the Iju and Sarkuh porphyry deposits in southeast Iran. Economic Geology, 108, 861-870.

Mohajjel, M., Fergusson, C.L., Sahandi, M.R., 2003. Cretaceous–Tertiary convergence and continental collision, Sanandaj-Sirjan Zone, Western Iran. Journal of Asian Earth Sciences, 21, 397-412.

Mohammaddoost, H., Ghaderi, M., Kumar, T.V., Hassanzadeh, J., Alirezaei, S., Stein, J.H., Babu, E., 2017. Zircon U–Pb and molybdenite Re–Os geochronology, with S isotopic composition of sulfides from the Chah-Firouzeh porphyry Cu deposit, Kerman Cenozoic arc, SE Iran. Ore Geology Reviews, 88, 384-399. DOI: https://mrdata.usgs.gov/sir20105090z/show–sir20105090z.php?id=9285

Moradian, A., 1997. Geochemistry, geochronology and petrography of feldspathoid-bearing rocks in Urumieh-Dokhtar volcanic belt, Iran. Ph.D. Thesis. Australia, University of Wollongong, 412pp.

Mineral Resources Data System (MRDS) USGS, 2015. Last accessed: November 2023. Website: https://mrdata.usgs.gov/sir20105090z/show-sir20105090z.php?id=9285

Mungall, J.E., 2002. Roasting the mantle: slab melting and the genesis of major Au and Aurich Cu deposits. Geology, 30, 915-918.

NICICo, 2010. Geology and alteration of Daralu area. Report of 1/1000 map exploration. Zarnab exploration consulting Company [in Persian]. Iranian Mines & Mining Industries Development & Renovation (IMIDRO), 78pp.

NICICo, 2021. Final report of exploration in the Daralu deposit. Kian Madan Pars & Sazeh Pardazi Iran Consulting Engineering Company, Tehran, internal reports, 150pp.

Ohmoto, H., Rye, R.O., 1979. Isotopes of sulfur and carbon. In: Barnes, H.L. (ed.). Geochemistry of Hydrothermal Deposits. John Wiley & Sons, 509-567.

Peacock, S.M., Rusher, T., Thompson, A.B., 1994. Partial melting of subducting oceanic crust. Earth and Planetary Science Letters, 121, 224-227.

Peccerillo, A., Taylor, S.R., 1976. Geochemistry of Eocene calc-alkaline volcanic rocks from Kastamonu area, northern Turkey. Contributions to Mineralogy and Petrology, 58, 63-81.

Pirajno, F., 2009. Hydrothermal processes and mineral systems. Springer, Geological Survey of Western Australia, 1250pp.

Pokrovski, G.B., Borisova, A.Y., Harrichoury, J., 2008. The effect of sulfur on vapor-liquid fractionation of metals in hydrothermal systems. Earth and Planetary Science Letters, 266, 345-362.

Profeta, L., Ducea, M.N., Chapman, J.B., Paterson, S.R., Gonzales, S.M.H., Kirsch, M., Petrescu, L., DeCelles, P.G., 2015. Quantifying crustal thickness over time in magmatic arcs. Scientific Reports, Nature Publishing Group, 17786.

Rapp, R.P., Watson, E.B., Miller, C.F., 1991. Partial melting of amphibolite/eclogite and the origin of Archaean trondhjemites and tonalites. Precambrian Research, 51, 1-25.

Rapp, R.P., Shimizu, N., Norman, M.D., Applegate, G.S., 1999. Reaction between slab-derived melts and peridotite in the mantle wedge: experimental constraints at 3.8 GPa. Chemical Geology, 160, 335-356.

Rapp, R.P., Xiao, L., Shimizu, N., 2002. Experimental constraints on the origin of potassium-rich adakite in east China. Acta Petrologica Sinica, 18, 293-311.

Richards, J.R., 2009. Postsubduction porphyry Cu–Au and epithermal Au deposits: products of remelting of subduction-modified lithosphere. Geology, 37, 247-250.

Richards, J.P., 2011. Magmatic to hydrothermal metal fluxes in convergent and collided margins. Ore Geology Reviews, 40, 1-26. DOI: https://doi.org/10.1016/j.oregeorev.2011.05.006

Richards, J.P., 2015. Tectonic, magmatic, and metallogenic evolution of the Tethyan orogen: from subduction to collision. Ore Geology Reviews, 70, 323-345. DOI: https://doi.org/10.1016/j.oregeorev.2014.11.009

Richards, J.R., Kerrich, R., 2007. Adakite-like rocks: their diverse origins and questionable role in metallogenesis. Economic Geology, 102(4), 537-576. DOI: https://doi.org/10.2113/gsecongeo.102.4.537

Richards, J.P., Boyce, A.J., Pringle, M.S., 2001. Geological evolution of the Escondida area, northern Chile: a model for spatial and temporal localization of porphyry Cu mineralization. Economic Geology, 96, 271-305.

Richards, J.P., Spell, T., Rameh, E., Razique, A., Fletcher, T., 2012. High Sr/Y magmas reflect arc maturity, high magmatic water content, and porphyry Cu ± Mo ± Au potential: examples from the Tethyan arcs of Central and Eastern Iran and Western Pakistan. Economic Geology, 107, 295-332.

Robb, L., 2005. Introduction to Ore-forming Processes. Oxford, Blackwell publishing, 1st edition, 386pp.

Rollinson, H.R., 1993. Using geochemical data: evaluation, presentation, interpretation. Singapore, Longman Singapore Publishers (Pte) Ltd, 1-352.

Rusk, B.G., Reed, M.H., Dilles, J.H., 2008. Fluid inclusion evidence for magmatic-hydrothermal fluid evolution in the porphyry copper-molybdenum deposit at Butte, Montana. Economic Geology, 103, 307-334. DOI: http://dx.doi.org/10.2113/gsecongeo.103.2.307

Seedorff, E., Dilles, J.H., Proffett, J.M.Jr., Einaudi, M.T., Zurcher, L., Stavast, W.J.A., Johnson, D.A., Barton, M.D., 2005. Porphyry deposits: Characteristics and origin of hypogene features. Society of Economic Geologists, Economic Geology 100th Anniversary 1905-2005, 251-298.

Shafiei, B., Haschke, M., Shahabpour, J., 2009. Recycling of orogenic arc crust triggers porphyry Cu mineralization in Kerman Cenozoic arc rocks, southeastern Iran. Mineralium Deposita, 44, 265-283.

Shahabpour, J., 1992. Unroofing fragmentites as a reconnaissance exploration tool in the central Iranian porphyry copper belt. Economic Geology, 87, 1599-1606.

Shahabpour, J., 2005. Tectonic evolution of the orogenic belt in the region located between Kerman and Neyriz. Journal of Asian Earth Sciences, 24, 405-417.

Shanks, W.C., 2014. Stable Isotope Geochemistry of Mineral Deposits. U.S. Geological Survey, Treatise on Geochemistry 2nd Edition, 59-82. DOI: http://dx.doi.org/10.1016/B978–0–08–095975–7.01103–7

Shepherd, T.J., Rankin, A.H., Alderton, D.H.M., 1985. A practical guide to fluid inclusion studies. London, Blackie Press, 239pp.

Sillitoe, R.H., 2010. Porphyry copper systems. Economic Geology, 105, 3-41.

Simmons, F.S., Browne, P.R.L., 2000. Hydrothermal Minerals and Precious Metals in the Broadlands-Ohaaki Geothermal System: Implications for Understanding Low-Sulfidation Epithermal Environments. Economic Geology, 95(5), 971-999.

Sinclair, W.D., 2007. Porphyry deposits. In: Goodfellow, W.D. (ed.). Mineral deposits of Canada: A Synthesis of Major Deposit-Types, District Metallogeny, the Evolution of Geological Provinces, and Exploration Methods. Newfoundland (Canada), Geological Association of Canada, Mineral Deposits Division, 5 (Special Publication), 223-243.

Singer, D.A., Berger V.I., Moring B.C., 2008. Porphyry copper deposits of the word: Database and grade and tonnage models. U.S. Geological Survey, Open-File Report 1155, 45pp.

Stocklin, J., 1968. Structural history and tectonics of Iran: a review. American Association of Petroleum Geologists, 52 (Bulletin), 1229-1258.

Sun, S., McDonough, W.F., 1989. Chemical and isotopic systematics of oceanic basalts: implications composition and processes. Geological Society. 42, 313-345.

Taghipour, N., 2007. The Application of Fluid Inclusions and Isotope Geochemistry as Guides for Exploration, Alteration and Mineralization at the Miduk Porphyry Copper Deposit, Shar-e-Babak, Kerman. Ph.D Thesis. Kerman (Iran), Shahid Bahonar University of Kerman, 305pp.

Topuz, G., Okay, A.I., Altherr, R., Schwarz, W.H., Siebel, W., Zack, T., Satır, M., Şen, C., 2011. Post collisional adakite-like magmatism in the Ağvanis Massif and implications for the evolution of the Eocene magmatism in the Eastern Pontides (NE Turkey). Lithos, 125, 131-150.

Van den Kerkhof, A.M., Hein, U.F., 2001. Fluid inclusion petrography. Lithos, 55, 27-47.

Wagner, T., Boyce, A.J., Jonsson, E., Fallick, A.E., 2004. Laser microprobe sulphur isotope analysis of arsenopyrite: experimental calibration and application to the Boliden Au-Cu-As massive sulphide deposit. Ore Geology Reviews, 25, 311-325.

Wallace, P.J., 2005. Volatiles in subduction zone magmas: concentrations and fluxes based on melt inclusion and volcanic gas data. Journal of Volcanology and Geothermal Research, 140, 217-240.

Wang, Q., Xu, J.F., Jian, P., Bao, Z.W., Zhao, Z.H., Li, C.F., Xiong, X.L., Ma, J.L., 2006. Petrogenesis of adakitic porphyries in an extentional tectonic setting, Dexing, South China: implications for the genesis of porphyry copper mineralization. Journal of Petrology, 47, 119-144.

Wang, R., Zhu, D., Wang, Q., Hou, Z., Yang, Z., Zhao, Z., Mo, X., 2020. Porphyry mineralization in the Tethyan orogeny. Science China Earth Sciences, 63, 2042-2067. DOI: 10.1007/s11430-019-9609-0

Whitney, D.L., Evans, B.W., 2010. Abbreviations for names of rock-forming minerals. American Mineralogist, 95(1), 185-187.

Wilkinson, J.J., 2001. Fluid inclusions in hydrothermal ore deposit. Lithos, 55, 229-272.

Xiao, L., Clemens, J.D., 2007. Origin of potassic (C-type) adakite magmas: experimental and field constraints. Lithos, 95, 399-414.

Xiong, X.L., Li, X.H., Xu, J.F., Li, W.X., Zhao, Z.H., Wang, Q., 2003. Extremely high-Na adakite-like magmas derived from alkali-rich basaltic underplate: the late Cretaceous Zhantang andesites in the Huichang Basin, SE China. Geochemical Journal, 37, 233-252.

Xiong, X.L., Xia, B., Xu, J.F., Niu, H.C., Xiao, W.S., 2006. Na depletion in modern adakites via melt/rock reaction within the sub-arc mantle. Chemical Geology, 229, 273-292.

Yan Wang, C., Zhou, F.Z., Qi, L., 2007. Permian flood basalts and mafic intrusions in the Jinping (SW China)-Song Da (northern Vietnam) district: mantle sources, crustal contamination and sulfide segregation. Chemical Geology, 243, 317-343.

Yang, Z., Hou, Z., Song, Y., Li, Z., 2008. Geology of the Qulong copper-molybdenum deposit, Tibet. Oslo, August 6–14, 33rd International Geological Congress.

Yang, Y.F., Chen, Y.J., Li, N., Mi, M., Xu, Y.L., Li, F.L., Wan, S.Q., 2013. Fluid inclusion and isotope geochemistry of the Qian'echong giant porphyry Mo deposit, Dabie Shan, China: a case of NaCl-poor, CO2-rich fluid systems. Journal of Geochemical Exploration, 124, 1-13.

Zarasvandi, A., Rezaei, M., Sadeghi, M., Lentz, D., Adelpour, M., Pourkaseb, H., 2015. Rare earth element signatures of economic and sub-economic porphyry copper systems in Urumieh-Dokhtar magmatic arc (UDMA), Iran. Ore Geology Reviews, 70, 407-423.

Zarasvandi, A., Rezaei, M., Raith, J.G., Asadi, S., Lentz, D., 2019. Hydrothermal fluid evolution in collisional Miocene porphyry copper deposits in Iran: Insights into factors controlling metal fertility. Ore Geology Reviews, 105, 183-200. DOI: https://doi.org/10.1016/j.oregeorev.2018.12.027

Zhang, Y., Frantz, J.D., 1987. Determination of the homogenization temperatures and densities of supercritical fluids in the system NaCl-KCl-CaCl2-H2O using synthetic fluid inclusions. Chemical Geology, 64, 335-350.

Zürcher, L., Bookstrom, A.A., Hammarstrom, J.M., Mars, J.C., Ludington, S., Zientek, M.L., Dunlap, P., Wallis, J., 2019. Tectonomagmatic evolution of porphyry belts in the central Tethys region of Turkey, the Caucasus, Iran, western Pakistan and southern Afghanistan. Ore Geology Reviews, 111, 102849. DOI: https://doi.org/10.1016/j.oregeorev.2019.02.034

Manuscript received October 2022;
revision accepted October 2023;
published Online December 2023.

APPENDIX I

TABLE I. Characteristics of vein groups in the Daralu deposit

Samples code	Dau 32	Dau 39	Dau 42	Dau 251	Dau 379	Dau 98	Dau 113	Dau 116	Dau 156	Dau 186	Dau 214	Dau 217	Dau 230
Wt.%													
SiO_2	58.9	61.37	59.44	70.75	69.76	56.78	67.65	58.9	61.73	59.44	68.66	59.13	62.82
TiO_2	0.59	0.47	0.59	0.17	0.31	0.67	0.32	0.59	0.47	0.59	0.23	0.64	0.42
Al_2O_3	18.47	16.52	17.35	10.48	9.73	16.76	14.13	18.47	16.52	17.35	14.11	16.82	16.4
FeO	4.84	5.17	4.45	6.56	7.07	5.96	4.21	5.58	6.04	5.84	3.96	5.81	4.25
MnO	0.04	0.04	0.13	0.03	0.02	0.07	0.03	0.04	0.04	0.13	0.07	0.05	0.03
MgO	1.17	1.13	2.77	0.46	1.26	1.73	1.21	1.17	1.13	2.77	0.67	1.47	0.82
CaO	5.05	4.07	4.06	1.53	3.47	5.73	4.1	5.05	4.07	4.06	2.29	4.5	4.07
Na_2O	5.25	3.74	4.6	2.98	3.36	4.59	4.44	5.25	3.74	4.6	4.91	4.27	3.55
K_2O	3.02	3.12	2.99	2.69	1.55	2.13	1.87	3.02	3.12	2.99	3.37	3.08	3.11
P_2O_5	0.15	0.15	0.15	0.04	0.07	0.16	0.08	0.16	0.16	0.16	0.04	0.17	0.14
Total	97.48	95.78	96.53	95.69	96.6	94.58	98.04	98.23	97.02	97.93	98.31	95.94	95.61
Mg#	34.15	24.20	26.26	22.85	37.86	30.40	35.38	24.63	35.64	41.90	25.47	27.84	26.71
ASI	1.09	1	1.07	1.02	1.01	1.02	1	0.91	1	1.02	0.93	0.93	1.03
ppm													
Be	1.5	1.3	1	0.9	1	0.8	0.5	1	1.1	0.6	0.7	0.7	1
Sc	4.3	9.3	11.5	3.7	7.1	8.3	5.4	6.2	3	8.5	4	7.5	4
V	67	96	94	23	64	115	61	100	66	113	27	93	59
Cr	4	25	22	13	12	40	7	23	4	32	8	24	7
Co	5.5	16.8	11.8	1.3	13.3	14.6	13.9	17.2	5.8	9.3	3.6	12.4	4.6
Ni	2	16	17	4	5	24	4	16	3	21	3	18	4
Zn	55	133	59	36	37	69	26	131	59	105	70	63	51
Rb	68	56	60	56	16	40	24	56	61	49	53	60	58
Sr	479	595	482.4	181.4	258.7	521.3	248.8	524	405.4	319	215.8	442.2	537.1
Y	2.6	4.6	9.3	9.9	5.6	7.5	4.3	4.6	2.5	9.8	12.1	8.4	2.9
Yb	0.4	0.6	1	0.9	0.5	0.9	0.4	0.6	0.2	1	1	0.9	0.2
Zr	82	79	74	5	5	69	5	76	57	5	5	65	27
Nb	5.4	5.8	5.8	1.9	1.8	4	2.8	4.1	3	3.2	2.2	2.8	3
Cs	38.1	4.3	7.8	2.5	3.3	6.6	2.6	3.5	31.2	6	2.5	6.3	5.1
Ba	525	490	347	463	146	340	124	442	460	406	529	300	473
La	28	21	19	11	12	22	18	20	26	16	20	17	21
Ce	47	35	35	21	21	37	23	33	45	25	29	32	34
Pr	4.18	2.71	3.62	3.01	2.3	2.49	1.2	1.84	2.86	1.65	1.75	2.34	2.32
Nd	15.6	10.6	15.8	9	7	10.3	4.6	7.2	10.5	7.2	6.8	9.7	9
Sm	1.92	1.17	2.55	1.43	0.2	1.53	0.22	1	1.37	1.24	1.27	1.56	1.24
Eu	0.79	0.74	0.93	0.49	0.1	0.7	0.38	0.66	0.67	0.54	0.6	0.69	0.62
Gd	1.42	1.29	2.64	2.53	2.25	1.88	1.14	1.4	1.54	1.72	1.69	1.9	1.46
Tb	0.2	0.25	0.39	0.27	0.15	0.27	0.17	0.2	0.18	0.32	0.31	0.31	0.19
Dy	0.74	0.9	3.58	2.43	1.66	1.21	0.63	0.77	0.44	1.55	1.63	1.42	0.43
Er	0.22	0.45	1.11	1.1	0.59	0.85	0.51	0.56	0.36	1.09	1.17	0.95	0.41
Tm	0.1	0.1	0.16	0.2	0.12	0.1	0.1	0.1	0.1	0.15	0.18	0.12	0.1
Yb	0.4	0.6	1	0.9	0.5	0.9	0.4	0.6	0.2	1	1	0.9	0.2
Lu	0.1	0.1	0.13	0.17	0.1	0.1	0.1	0.1	0.1	0.13	0.16	0.11	0.1
Hf	2.49	2.8	3.06	0.5	0.5	2.22	0.75	2.4	1.99	0.79	0.78	2.29	1.4
Ta	0.45	0.55	0.47	0.6	0.45	0.52	0.57	0.57	0.4	0.5	0.4	0.36	0.41
Pb	17	15	23	1	1	13	7	16	21	29	13	12	15
Ti	3053	3796	4101	1050	1892	4017	1918	3537	2818	3537	1379	3837	2518
Th	6.69	7.52	4.35	4.05	4.56	5.2	3.83	6.01	5.11	5.29	3.89	3.5	3.79

Samples code	Dau 32	Dau 39	Dau 42	Dau 251	Dau 379	Dau 98	Dau 113	Dau 116	Dau 156	Dau 186	Dau 214	Dau 217	Dau 230
Wt.%													
U	1.7	1.9	1.1	0.3	0.5	1.48	0.4	1.8	1.5	1.1	0.4	1	0.6
Eu/Eu*	1.41	1.78	1.06	0.76	1.39	1.22	2.25	1.6	1.3	1.09	1.21	1.18	1.36
Nb/Ta	12	10.54	12.34	3.1	4	7.6	4.9	7.1	7.5	6.4	5.5	7.77	7.31
Sr/Y	184.03	129.34	51.87	18.32	46.19	69.50	57.86	113.91	162.16	32.57	17.83	52.64	185.20
La/Yb	70	35	19	12.22	24	24.4	45	33.33	130	16	20	18.88	105
Zr/Sm	42.70	67.52	29.01	3.49	25	45.09	22.72	76	41.60	4.03	3.9	41.66	21.77
La/Sm	14.58	17.94	7.45	7.69	60	14.37	81.81	20	18.97	12.90	15.74	10.89	16.93
Sm/Yb	4.8	1.95	2.55	1.58	0.4	1.7	0.55	1.66	6.85	1.24	1.27	1.73	6.2
$(La/Sm)_n$	9.41	11.58	4.81	4.96	37.2	9.28	15.27	12.91	12.25	8.32	10.16	7.03	10.93
$(Dy/Yb)_n$	1.23	1	0.91	1.14	2.22	0.89	1.05	0.85	1.47	1.03	1.09	1.05	0.71

ASI= molar $Al_2O_3/(CaO+K_2O+Na_2O)$, Mg# numbers= $(100\times MgO/(MgO+0.9FeO_t))$, $Eu^*= \sqrt{Sm_n+Gd_n}$